Chapter 1

Introduction

1.1 Background and overview of low temperature poly-Si(LTPS) TFTs technology

Polycrystalline silicon thin-film transistors (poly-Si TFTs) become much more applicable in active matrix liquid crystal displays (AMLCDs)[1]-[3] in recent years, and in some memory devices such as dynamic random access memories (DRAMs)[4], static random access memories (SRAMs)[5], electrical programming read only memories (EEPROMs)[6], and electrical erasable programming read only memories (EPROMs)[7]. Furthermore, several linear image sensors[8], thermal printer heads [9], photodetector amplifier [10], and three dimension LSIs [11] have also adopted poly-Si TFTs technology.

Unlike amorphous silicon (a-Si) TFTs, poly-Si TFTs have much larger carrier mobility which usually exceeds 100 cm^2 / Vs by present mature technology. Its superior carrier mobility is essential to successfully integrate polys-Si TFTs and peripheral driving circuits [5] on the same panel to reduce the assembly complexity and cost. Therefore, the low process temperature of poly-Si TFTs with the high mobility makes it possible to realize the ultimate goal, system-on-panel [12]. Furthermore, due to the higher mobility of poly-Si TFTs, the dimension of the poly-Si TFTs can be made smaller than that of a-Si TFTs to achieve high density and high resolution AMLCDs.

However, there are still some problems existed in poly-Si TFTs. Compared to single crystalline silicon, poly-Si has a lot of defects at the grain boundaries. These defects,

regarding as trap states, locate in the disordered grain boundary region and degrade device performance severely. In other words, the performances of poly-Si TFTs are strongly affected by the grain structure inside the channel region. Thus, the larger grain with less grain boundary defects is desirable and currently many researches attempting to achieve this goal have been studied, such as solid-phase crystallization (SPC)[13], metal-induced-lateral crystallization (MILC)[14] and laser crystallization [15]. As a result, one of the major barriers in developing the technology lies in the growth of poly-Si grains with high uniformity and large grain size at the same time.

In summary, the poly-Si TFTs will play an important role in many aspects in the future, especially as the three-dimensional circuit era is coming.

There are three main methods used in LTPS we mention above :(1) Solid phase crystallization (SPC), (2) metal induced lateral crystallization (MILC) (3) Laser crystallization (LC):
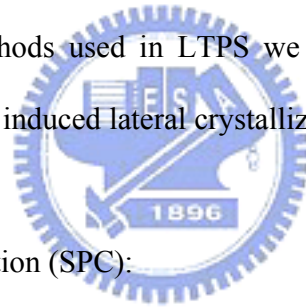
 (1) Solid phase crystallization (SPC):

 The most direct method to obtain polysilicon films is heat the amorphous silicon films in a furnace. Amorphous silicon is a thermodynamically metastable phase. When the silicon film obtains a sufficient energy to overcome the initial energy barrier, the amorphous silicon starts to transfer to polysolicon. The SPC could be accomplished in a wide temperature process window corresponding to annealing times. The relation between annealing temperature and annealing time is not unique[16] , since the micro structural details of the precursor-Si film play a important rule. With different deposition method and conditions[17.18], the nucleation rate would be strongly influenced. By increasing the deposition rate and the decreasing the temperature, the silicon film will

form a violent structural disorder that induces the silicon hard to nucleation.

(2) Metal induced lateral crystallization (MILC):

In MILC, the enhancement in grain growth is attributed to an interaction of the free electrons if the metal with covalent silicon bonds at the growing interface. MILC makes the amorphous crystallized in a lower temperature than that of SPC. At first, a nickel film was deposited on the amorphous silicon, with the increasing the temperature, the silicon and nickel combined to the formation of NiSi and $NiSi_2$, and at the temperature in the range of 450-700°C the NiSi transforms into thermodynamically favored phase, $NiSi_2$. The disilicide $NiSi_2$ is cubic with the CaF_2 structure and has a very close lattice constant match to c-Si. The nickel is the dominant diffusion species in NiSi and $NiSi_2$ such that the nickel diffused and left the silicon in a polysilicon phase. The diffusion of the nickel induced a lateral crystallization. As the result of such growth mechanism, silicide-mediated polysilicon films demonstrate a fibrous microstructure, with each fiber attributed to c-Si growth from an individual disilicide precipitate. An important problem in MILC is that there is still some residual nickel in the MILC region. MILC also has been combined with laser crystallization technology[19]. Figure 1-1-1(a) is the structure and fabrication process of combining MILC and ELA[20]. Figure 1-1-1 (b) and (c) are SEM images with different laser intensity.

(3) Laser crystallization (LC):

By using a laser, the silicon film could be heated in a certain section expected, and the substrate temperature can also be controlled less than the deformation threshold even on a plastic substrate with a thicker SiO_2 insulator layer. As the silicon film absorbs the

laser light, the high laser energy not only heats the film to the melting temperature but transfer the extra-energy to the latent heat of the silicon to melting the film. Several nanoseconds later, the melted silicon film releases the energy into the substrate. At the same time liquid-phase silicon solidifies and transfers into the polysilicon. The microscopic structure of the laser-crystallized poly-Si films depends on a variety of parameters such as film thickness, laser energy density, and laser wavelength.

By SEM measurements, it could be found that the average grain size is strongly affected by the laser energy density used for the crystallization. At the low laser energy density, the average grain size increases with increasing laser intensity. This energy regime is known as the partial melting fluence. In this laser intensity regime, the average grain size is confined due to the large number of the nuclei and the low energy. At the high laser fluence, the average grain size is not proportional to the laser energy. This energy range is referred to as the complete melting fluence. In such regime, there is a supercooling governing the solidification of silicon. When the supercooling occurs, a great number of nuclei appear in the film such that the average grain size decreases to about 0.1μm dramatically. Between above two regimes, the third laser fluence is called as super lateral growth (SLG) regime. When the laser energy density just reaches the intense to completely melt the silicon film, there are only a few discontinuous and non-melted residual silicon islands existing in the bottom of the film, and the grain grow from the nuclei. The solid-liquid phase moves laterally in the film, and the average grain size about several times the film thickness could be obtained. However, the process window of SLG is too narrow to control precisely. If laser intensity shifts, the crystallized polysilicon film will not keep in the SLG regime but transfer to the others. The

crystallization phenomenon of three regimes we mentioned above is shown in Fig.1-1-2, and the relation between the laser fluence and the grain size is shown in Fig. 1-1-3.

1.2 Introduction of amorphous carbon (a-C:H)

DLC consists not only of the amorphous carbons (a-C) but also of the hydrogenated alloys, a-C:H. It is convenient to display the compositions of the various forms of amorphous C---H alloys on a ternary phase diagram as in fig.1-2-1.There are many a-Cs with disordered graphitic ordering, such as soot, chars, glassy carbon, and evaporated a-C. These lie in the lower left hand corner. The two hydrocarbon polymers polyethylene $(CH_2)_n$ and polyacetylene $(CH)_n$ define the limits of a triangle in the right hand corner beyond which interconnecting C---C networks cannot form, and only molecules form. Deposition methods have been developed to produce a-Cs with increasing degrees of sp^3 bonding. Sputtering can extend from sp^2 bonding some way towards sp^3 bonding. If the fraction of sp^3 bonding reaches a high degree, the a-C is denoted as tetrahedral amorphous carbon (ta-C), to distinguish it from sp^2 a-C. A range of deposition methods, such as plasma enhanced chemical vapour deposition (PECVD), is able to reach into the interior of the triangle. This produces a-C:H.

Carbon usually exists in several forms; graphite, diamond, and the new form of fullerines. Various carbon forms with different characteristic were based on the bonding order of the carbon atoms. Amorphous carbon (a-C:H) was a structure containing both sp^2 and sp^3 bondeding.

The a-C:H was usually used as the liquid crystal (LC) alignment layer, passivation layer for machine, V low-k and interlayer dielectric films in the integrate circuit (IC)

device. The a-C:H film had good optical absorbance over a wide wavelength. The a-C:H films was a good candidate to be a heat retaining layer due to its low thermal conductivity and high heat capacitance.

1.3 Motivation

Laser crystallize technologies by excimer laser have been extensively studies. To increase the carrier mobility and reduce the leakage current, a giant silicon grain was claimed to reduce the amounts of the grain boundary. Many ways were published to enlarge the silicon grain. To extend the melting time and let the silicon grown to be a giant silicon grain, a new material a-C:H was chosen to be a heat retaining material in this thesis. The heat retaining material would extend the silicon molten time and decreased the cooling rate.

The heat retaining layer used in the thesis was a-C:H. Compared to Si_3N_4 and SiONx, a-C:H had a high absorption coefficient and low thermal conductivity. The heat characteristic of a-C:H would let the melting temperature and melting time of the silicon film increased. A giant silicon grain would be formed when the silicon crystallized with a high melting temperature and long melting time.

Chapter 2

Fabrication process and Heat Flux Simulation

2.1 Thin film deposition

2.1.1 Silicon oxide formation

First, the silicon wafer was cleaned by standard RCA clean. The steps were followed by dipping NH_4OH ($NH_4OH：H_2O_2：H_2O = 1：4：20$) at $75°C$ for 10 minutes, dipping the HCl ($HCl：H_2O_2：H_2O = 1：1：6$) at $75°C$ for 10 minutes ,and then dipping the HF($HF：H_2O = 1：100$) at $25°C$ for 10 seconds. The silicon oxide is deposited by horizontal furnace (APCVD wet oxide) at $980°C$ for 7 hours and 40 minutes on the cleaned silicon wafer. The thickness of silicon oxide was about 1um measured by the n&k analyzer.
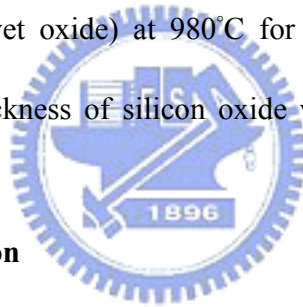
2.1.2 a-C:H film formation

After depositing the silicon oxide, the amorphous carbon (a-C:H) was deposited by plasma-enhanced chemical vapor deposition (PECVD) under the RF power of 100W for 30 minute. The a-C:H film was formed by hydrogen (H_2) and methane (CH_4) of the flow rate: 10.3$sccm$ with the ratio of 1:1 under the pressure of 18$mtorr$. The deposition rate of a-C:H films was about 200nm/hr. The thickness of a-C:H was measured by N&K analyzer.

2.1.3 Amorphous silicon formation

Amorphous silicon film was deposited by sputter in the process temperature — $38°C$. The deposition rate of amorphous silicon was about 0.01nm/sec for the thickness of

100nm. The silicon film was defined by the patterned photo resist and etched by the system of poly-Si RIE (poly-Si reactive ion etching system).

2.2 Material analysis

2.2.1 The absorption coefficient (α)

The amorphous carbon (a-C:H) film was chosen to be a heat retaining layer due to its strong optical absorption ability in a wide range of wavelength. The a-C:H film was suitable to be a heat retaining layer for various laser instruments, such as excimer laser and solid state green laser.

The absorbency of a-C:H was measured by N&K analyzer and analyzed by the equation published by [21]. Various absorptivity of the a-C:H film were obtained when incident wavelength was altered. The result of the absorptivity was shown in Fig.2-2-1. The a-C:H film with 100 nm was used to measure the absorbency of a-C:H.

The optical absorption coefficients was determined by [22]

$$\alpha = \frac{4\pi k}{\lambda} \qquad \text{Eq.2.1}$$

and

$$A = (1-R)(1 - \exp^{-\alpha x}) \qquad \text{Eq.2.2}$$

In the equation, α is the absorption coefficient, λ is the wavelength of laser, A is the absorptivity, k is extinction coefficient, and R is reflectance. By the analysis, the absorbency of a-C:H at 532nm was 48% and 351nm was 79.8%. As to the most popular XeF excimer laser, a-C:H film shows a strong superiority to be a candidate of heat retaining layer of excimer laser. Therefore, a-C:H can help us to store a lot of heat when

the laser irradiates. The absorbency of a-C:H film is large at 351nm and 532nm. So the a-C:H film shows good optical absorbance over a wide wavelength.

2.2.2 SEM

The scanning electron microscope (SEM) was a type of electron microscope capable of producing high-resolution images of a sample surface. Due to the manner in which the image is created, SEM images have a characteristic three-dimensional appearance and are useful for judging the surface structure of the sample.

These samples used in this thesis were irradiated with different laser energy density of 150-400mJ/cm^2.Before the sample analyzed by SEM, the secco etching was done for 90 seconds to etch the grain boundary. The components of the liquid for seeco etching are HF and $K_2Cr_2O_7$.

2.2.3 Raman spectrum

Raman spectroscopy offers several advantages for microscopic analysis. Since it is a scattering technique, specimens do not need to be fixed or sectioned. Raman spectra can be collected from a very small volume (< 1 μm in diameter). So Raman is a very useful tool for analyzing the component of amorphous carbon (a-C:H). The Raman spectrum component of a-C:H was shown in fig. 2-2-2 [23]. There are two important Raman peaks of a-C:H films: the D-band at 1360 cm^{-1} associated with disorder and the G-band at 1580 cm^{-1}~1600 cm^{-1} associated with sp^2-bond vibration (graphite).The 1332 cm^{-1} represents diamond, and the 1580 cm^{-1} represents the perfect crystallization of graphite. The components of the a-C:H are mixed with D-band and G-band. When the G-band peak position is shifted from 1580 cm^{-1} to 1600 cm^{-1}, the micro-crystalline graphite phase gradually formed.. As shown in fig.2-2-2, the D-band peak and the G-band peak were

apparently and impendent when the micro-crystalline graphite phase was formed.

2.3 Heat flux analysis

The software used to simulate the laser crystallization process is FEMLAB which was a interactive environment for modeling and solving many kinds of scientific and engineering problems based on partial differential equations (PDEs). One of the tools is heat transfer simulation, and we choose the mode – transient analysis but not the steady state because we would try to analyzing the full process of the laser crystallization. We define the mesh shape to be triangle illustrated in figure 2-3-1, and the mesh density increasing would add our simulation time and the precision of the results simultaneously. We set each time step to be 1ns and the total simulation time to be 800ns such that we could confirm the accuracy and the completeness of the results at the same time. The following example will illustrate a simple simulation about the laser crystallization.

The heat flow in a simple structure shown in Figure 2-3-2 with the labeled dimensions was simulated. The boundary conditions are then written as

$$\partial T/\partial x \mid_{x=0} = 0 , \qquad \partial T/\partial x \mid_{x=3um} = 0$$

$$\partial T/\partial y \mid_{y=1.1um} = 0 , \qquad T\mid_{t=0s} = T_s = 23℃$$

where T is the temperature and the T_s is the ambient temperature and the initial sample temperature. The initial condition is $T\mid_{t=0s} = T_s = 23℃$ for all regions. An equation at time t is $c \cdot (\partial T/\partial t) = \nabla \cdot (k\nabla T) + Q$, where c and κ are specific heat and thermal conductivity, respectively. Q is the heat generation or loss rate per unit volume.

The effects of infrared light emission and absorption were neglected in this simulation. The heat generation was only coursed by the absorption of the excimer laser

light. The absorption coefficient α measured by n&k analyzer was relative to the wavelength of the incident laser. The absorption coefficient was influenced by the process temperature, but it was ignored in this thesis. The value of the absorption coefficient in this thesis was fixed to 0.7cm^{-1}. The part of the laser light irradiation was represented as the following equation:

absorption $= T \times \alpha \, I_0(t,y) \exp(\alpha \, (y_0\text{-}y))$

where y_0 is the position at the top of the α-Si film ,I_0 is the light intensity irradiated to the sample surface and T is the transition coefficient. I_0 is assumed a square-like time dependence that takes a constant value from t=0s to t=20ns. The additional heat stored and released is in the silicon film during the crystallization process. The temperature regime from 1350 to 1440^OC is setting for the latent heat stored in the silicon film at t<20ns (during laser irradiation) and released at t>20ns (after laser irradiation). The value of latent heat is 3000J/cm^3 and other parameters such as specific heat, thermal conductivity···etc. were list in table I [24]

The simulation results includes the temperature curve of a particular point versus the time, the temperature curve of a particular line versus the time, the thermal distribution at a certain time, the contour lines of the temperature at a certain time and the heat flux at a certain time. The results mentioned above will be illustrated in figure 2-3-3. From the temperature curve of a particular point versus the time we could understand the state of the silicon and from the contour lines of the temperature at a certain time and the heat flux at a certain time we could know the grain growth direction which is in the anti-direction of the heat flux. In figure 2-3-3(b) there is no other special design, the laser

energy tends to transfer to the substrate such that the grain would grow form the interface of two layers to the top surface vertically. In figure2-3-3 (c) there exists a thermal platform region which represents the latent heat releasing during the liquid-phase Si transferring to solid-state Si. By analyzing figure 2-3-3 (d) the conclusion could be obtained is that after laser irradiation (at 20ns) the most energy absorbed by the α-Si layer. With the time passing, the exceeding heat transfer to the bottom SiO_2 layer the silicon film tends to be same in each depth due to the high thermal conductivity of Si. Four results above are useful tools to analyze the crystallization process.

Chapter 3

Result and Discussion

3.1 Excimer laser crystallization with the heat retain layer (HRL) - a-C:H

3.1.1 The absorption coefficient of a-C:H film

The absorption coefficient of heat retain layer (HRL) was very important for the amorphous silicon film crystallization. The heat would be absorbed and stored by the heat retain layer. A large poly-Si grain would be formed when the heat was retained to extend the crystal time.

A material with high absorption coefficient a-C:H was used to be a HRL in this thesis. The optimum condition was analyzed to fabricate a high absorption coefficient a-C:H. As calculated in Eq.2.1,Eq.2.2, the absorption coefficient and absorptivity was analyzed by n&k analyzer and listed in Table II. As listed in Table II, the wave length was 351nm for XeF laser and 532nm for solid state green laser (Nd:YAG). By the limit of our laser instrument, the XeF (351nm) laser was used for our laser source. The largest absorption coefficient would be obtained when the input gas ratio hydrogen(H2)/methane(CH4) of 1/1, 30 minute and the RF power of 100W was used to deposit the a-C:H film. Therefore, we use this film as our heat retain layer (HRL). The a-C:H with absorption coefficient of 17150.3 cm^{-1} and the absorptivity of 79.8% for XeF laser was used as the heat retain layer of the laser crystallization.

3.1.2 The heat flux analysis of the silicon crystallized on different HRL

The software used to simulate the laser crystallization process was FEMLAB. All kinds of condition and structure would be simulated before the device was fabricated.

The result of the simulation would be an important reference for designing this experiment process. The simulated result for this experiment was discussed as below.

First, the temperature of the silicon film was simulated to analyze the heat flow condition when the laser energy density was modified from 100 mJ/cm^2 to 400 mJ/cm^2. As shown in Fig. 3-1-1 (a), the sandwich structure was used to analyze the heat flow condition. From the simulated result shown in Fig. 3-1-1 (b), the temperature of the silicon melting point would not achieve when the laser density was 100 mJ/cm^2. The laser density of 100 mJ/cm^2 was too low to crystallize the silicon film. When the laser energy density was up to the 150 mJ/cm^2, the temperature was high enough to melting and crystallizes the silicon film. The temperature of the silicon would be increased when the laser energy density was raised, and the temperature of 5467K would be achieved when the laser energy density was 400 mJ/cm^2. As shown in Fig. 3-1-1 (b), the latent heat time would increase when the laser density was increased. The increased latent heat time would help the time of the solid-liquid phase be extended. The a-Si would tend to grow a giant poly silicon grain when the time of the solid-liquid phase was long.

As presented in Fig. 3-1-2, various absorption coefficients were simulated to observe its latent heat time. The absorption coefficient of silicon oxide was 450 cm^{-1} and the absorption coefficient of a-C:H was 17150.3 cm^{-1}. The absorption coefficient of a-C:H was much larger than the absorption coefficient of silicon oxide. Therefore, the latent heat time of the silicon film on a-C:H was much larger than it on silicon oxide.

Otherwise, various structures were also designed to be simulated. As shown in Fig. 3-1-3.(a), the device was fabricated as the following process flow: 1um silicon oxide was deposited on the silicon-substrate by horizontal furnace (980 $^{\text{o}}$C), and the100nm a-C:H

and 100nm amorphous silicon were deposited respectively without any patterning. The a-C:H film was patterned by reactive ion etching (RIE) in a SF_6-CHF_3 plasma (30sccm:10sccm) before depositing the amorphous silicon in Fig. 3-1-3.(b). After a-C:H depositing, the amorphous silicon film was deposited and patterned in Fig. 3-1-3.(c). As simulated in Fig. 3-1-3.(d), the structure of Fig. 3-1-3.(d) would have a high temperature and long latent heat time in the silicon film. To crystallize a giant poly-Si grain, the structure of Fig. 3-1-3.(c) would be designed to crystallize by the excimer laser exposing.

The sample was irradiated by XeF excimer laser (wavelength of 351nm) with various laser energy density. The amorphous silicon film was melted and crystallized by the excimer laser. The amorphous silicon was deposited and patterned on the a-C:H film and silicon oxide film respectively in Fig. 3-1-4. The sample A was patterned amorphous silicon deposited on the a-C:H film and the sample B was that deposited on the silicon oxide film. As shown in Fig. 3-1-5 (a)~(p), the crystallized poly-Si grain after secco etching would be observed by scanning electron microscopy (SEM)..The laser energy density was spilt from175 mJ/cm^2 to 400 mJ/cm^2 . From the SEM image, the grain size of sample A and sample B was very small when the laser energy density was under 175 mJ/cm^2. However, the grain size of sample A would be larger than 100nm when the laser energy density was over 175 mJ/cm^2,. The grain size of sample B was too small to be recognized in the laser energy density 175 mJ/cm^2 .During the laser energy density of 175 mJ/cm^2 ~ 275 mJ/cm^2 , the grain size of sample A was larger than the grain size of sample B. The poly- Si grain on the heat retain layer (HRL) — a-C:H   would be larger than that on the silicon oxide film when the laser energy density was under 275 mJ/cm^2.

The poly- Si grain crystallized on the a-C:H would become smaller than that on the silicon oxide film when the laser energy density was over 300 mJ/cm^2 . The film of sample A would crack with the laser energy up to 400mJ/cm^2 .

Several rules could be used to make a description of the grain size variation when the laser energy density was higher than 275 mJ/cm^2. First, the laser energy density over 275 mJ/cm^2 was high enough to let the silicon film be complete-melting and form a small size fine grain in sample A . Even the silicon film cracked due to the temperature of the silicon film is too high. The temperature in sample B was not high enough to form a fine grain due to the low absorption coefficient of the silicon oxide film. Second, the a-C:H film might be modified to a different bonding mode by the high energy density. Final, a-C:H mixed with the silicon in the melting state during the process of the laser crystallization

3.2 Raman analysis

3.2.1 Raman analysis of the crystallized poly- Si film

The quality of the crystallized poly- Si was analyzed by the Raman spectra. A high speed and precise result of crystallization could be obtained by the Raman spectra. The Raman peak positions and FWHM of sample A were shown in Fig. 3-2-1. Generally, the Raman peak position of single crystalline silicon was located at 520.8 cm^{-1}. The crystalline quality would get much similar to a single crystalline when the Raman peak position approaches to 520.8 cm^{-1}. The uniformity of the crystallized poly- Si could be obtained by the FWHM of the Raman spectra. in Fig.3-2-1, the FWHM curve was reduced when the laser energy density was increased in lower laser energy density

region(175 mJ/cm^2 ~ 250 mJ/cm^2). And the peak position would approach to 520.8 cm^{-1} with increasing laser energy density. A high crystalline quality would be obtained when the laser energy density increased (in lower energy region). Otherwise, the FWHM was increased and the peak position was decreased when the laser energy density increased in high laser energy density region (>270 mJ/cm^2). The result of the Raman analysis was consist with the SEM images.

The Raman peak positions and FWHM of sample B were shown in Fig. 3-2-2. The FWHM curve would be reduced with increasing laser energy density (175 mJ/cm^2 ~ 350 mJ/cm^2). And the peak position approaches to 520.8 cm^{-1} with increasing laser energy density. By the analysis of the Raman spectrum in Fig. 3-2-3 and Fig. 3-2-4, the quality of crystallized poly-Si would be increased with increasing the laser energy density. These also correspond to the result of SEM images.

It can be found that the FWHM of sample A is smaller than the FWHM of sample B. It means that the sample A has the better crystalline quality than the sample B. However, the peak position of the sample A is far away the 520.8 cm^{-1} than the sample B. The result maybe the Raman signal of the silicon substrate mix with the signal of the poly-Si in the sample B.

The X_c (crystalline volume factor) could be calculated by the Raman spectra data. The Raman spectra of silicon film were composed of three peaks at around 480 cm^{-1}, 510 cm^{-1} and 520 cm^{-1}. The peaks at 480 cm^{-1} and 520 cm^{-1} imply to the amorphous phase and crystalline phase, respectively. [25][26] The peak at 510 cm^{-1} was reported to be the crystalline phase, even its origin was still unknown. X_c was given by the formula

$$X_c = (I_{510} + I_{520}) / (I_{480} + I_{510} + I_{520}) \qquad \textbf{Eq.3.1}$$

The crystalline volume factor was calculated and listed in Table.IV The X_c(crystalline volume factor) would increase with the laser energy density increasing. The X_c(crystalline volume factor) in sample A with the laser energy density of 275 mJ/cm^2 was up to 90.5% larger than the X_c (84.4%) in sample B. By the analysis result, the sample with heat retain layer would have a higher crystalline volume factor than that with silicon oxide..

3.2.2 Raman analysis of the a-C:H film

As shown in Fig.3-2-5, the Raman curve of the a-C:H after laser annealing would be modified. The Raman peak position of a-C:H was shifted from 1580 cm^{-1} to 1600 cm^{-1} when the laser energy density was higher than 200mJ/cm$^{2.}$.The bonding structure of the a-C:H was altered by the excimer laser exposing from the shifted Raman peak position. The intensity ratio of the G-band and D-band in Raman spectrum was proposed to analyze sp^2-band by ref [12]. As listed in Table.III (a), the ratio of the intensity of G-band and D-band was reduced when the laser energy density increased. It maybe the sp^2 banding was broken and the intensity of G-band was reduced. As published in ref[12], the reduced intensity ratio of G-band and D-band implied that some micro-crystalline graphite was formed. Therefore, the bonding structure and the thermal conductivity of the a-C:H were altered when the a-C:H was exposed by a high laser energy density – larger than 200mJ/cm^2. Some micro-crystalline graphite phase would also be observed in Fig.3-2-5 when the exposing laser energy was higher than 200 mJ/cm$^{2.}$. The Raman spectrum of a-C:H after laser exposing was consist with the SEM figure of crystallized poly-si. Due to the thermal conductivity increased when the a-C:H was crystallized, the silicon grain size was reduced when the laser energy was higher than 275 mJ/cm^2 .

Chapter 4

Conclusion

The simulating software FEMLAB was used to observe the heat flow during the laser crystallization process. The device with different conditions and structures was simulated and analysis. According to the results simulated by FEMLAB, the optimum conditions were chosen to crystallize the poly- Si. A heat retaining material a-C:H was introduced to extend the melting time in this thesis.

Compared by the result of the laser crystallization, a large grain size in low laser energy density was found when the poly-Si crystallized on the material with high absorption coefficient a-C:H. The SEM images and micro-Raman were used to analyze the crystallization of poly- Si grain. A large grain with high crystalline volume factor would be observed when the poly- Si was crystallized on the a-C:H film in low laser energy around 175 mJ/cm^2 ~ 275mJ/cm^2. A poly silicon with the Raman peak position about 516.7 cm^{-1} and the FWHM about 3.51 cm^{-1} was obtained by the suggested structure and heat retaining material a-C:H. However, when the laser energy density increased to be higher than 300 mJ/cm^2, the grain enlargement due to the HR material was diminished. By Raman analysis, it was found that the sp^2-band signal in a-C:H film was decreased. Since in a-C:H film, the destruction of the sp^2-band leads to the increase of the thermal conductance, the heat retaining property is therefore destroyed. As a result, the grain size of poly-Si film on the a-C:H film became smaller than without the a-C:H film.

In the future, the laser source with a long wavelength will be suggested to

crystallize the a-Si with the a-C:H film. As shown in Fig4-1, a-C:H had a high absorption coefficient in short wavelength (351 nm) and in long wavelength (> 532 nm). Amorphous-Carbon:H film was potential to be used as an H-REC layer in a long wavelength laser source, such as the solid state laser(532nm). As simulated in Fig.4-2 , the temperature of the silicon film and the a-C:H film are reduced in a long wavelength laser source. When the temperature of the a-C:H film are reduced, it can avoid the micro-crystalline graphite of the a-C:H formed. The crystallized graphite had higher thermal conductivity than the a-C:H film. To retain the heat in HR layer, a material with a low thermal conductivity had to be used. The temperature had to be lowered to prevent the graphite crystallized and keep its low thermal conductivity. Otherwise, the a-C:H molecule may diffuse to the a-Si film and be nuclei of the crystallized poli-Si. These nuclei may let the poly-Si be crystallized to fine grain with small grain size. The reduced temperature of the a-C:H film can also let the diffusing a-C:H be reduced. Therefore, the temperature of the silicon film and the a-C:H film are reduced in a long wavelength laser source. The fine grain and film ruptured will be reduced when the poly silicon is crystallized in near-complete melting temperature. Due to the high absorption coefficient of the a-C:H film in a long wavelength laser, the giant silicon grain is expected to be crystallized in the future.

References

[1]   A. G. Lewis, I-W. Wu, T. Y. Huang, A. Chiang, and R. H. Bruce, "Active matrix liquid crystal display design using low and high temperature processed polysilicon TFTs," in IEDM Tech. Dig., pp. 843-846, 1990

[2]   Y. Matsueda, M. Ashizawa, S. Aruga, H. Ohshima, and S. Morozumi, "New technologies for compact TFT LCDs with high-aperture ratio, "soc. Information Display, Tech. Dig., pp. 315-318, 1990.

[3]   R. G. Stewart, S. N. Lee, A. G. Ipri, D. L. Jose, D. A. furst, S. A. Lipp, and W. R. Roach, "A 9V polysilicon LCD with integrated gray-scale drivers," soc. Information Display, Tech. Dig., pp. 319-322, 1990.

[4]   T. Yamanaka, T. Hashimoto, N. Hasegawa, T. Tanaka, N. Hashimoto, A. Shimizu, N. ki, K. Ishibashi, K. Sasaki, T.Nishida, T. Mine, E. Takeda, and T. Nagano, "Advanced TFT SRAM Cell Technology Using a Phase-Shift Lithography," IEEE Trans. Electron Devices, Vol. 42, No. 7, pp. 1305-1313, 1995.

[5]   S. D. S. Malhi, H. Shichijio, S.K. Banerjee, R. Sundaresan, M. Elahy, G. P. Polack, W. F. Richardaon, A. h. Shah, L. R. Hite, R. H. Womoack, P. K. Chatterjee, and H. W. Lan, "Characteristics and Three-Dimensional Integration of MOSFETs in Small-Grain LPCVD Polycrystalline Silicon," IEEE Trans. Electric Devices, Vol. 32, No. 2, pp. 258-281, 1985.

[6]   K. YoShizaki, H. Takahashi, Y. Kamigaki, T.Yasui, K. Komori, and H. Katto, ISSCC Digest of tech. Papers, pp. 166, 1985.

[7]   N. D. Young, G. Harkin, R. M. Bunn, D. J. McCullloch, and I.D. French, "The Fabrication and Characterization of EEPROM Arrays on Glass Using a Low-Temperature Poly-Si TFT Process," IEEE Trans. Electron Devices, Vol. 43,

No.11, pp. 1930-1936, 1996.

[8]   T. Kaneko, Y. Hosokawa, M. Tadauchi, Y. Kita, and H. Andoh, "400 dpi Integrated Contact Type Linear Image Sensors with poly-Si TFT's Analog Readout Circuits and Dynamics shift Registers," IEEE Trans. Electron Devices, Vol. 38, No. 5 ,pp. 1086-1039, 1991.

[9]   Y. Hayashi, H. Hayashi, M. Negishi, T. Matsushita, "A Thermal Printer Head with CMOS Thin-Film Transistors and Heating Elements Integrated on a Chip," IEEE Solid-State Circuits Conference (ISSCC), pp. 266, 1998.

[10]   N. Yamauhchi, Y. Inaba, and M. Okamamura, "An Integrated Photodector-Amplifier using a-Si p-i-n Photodiodes and Poly-Si Thin Film Transistors, " IEEE Photonic Tech. Lett., Vol. 5, pp. 319, 1993.

[11]   K. Nakazawa, "Recrystallization of amorphous silicon films deposited by low-pressure chemical vapor deposition from Si_2H_6 gas," J. Appl. Phys.,Vol. 69, pp. 1703-1706, 1991.

[12]   T. Serikawa, S. Shirai, A. Okamoto, and S. Suyama, "Low-temperature fabrication of high-mobility poly-Si TFTs for large-area LCDs," IEEE Trans. Electron Devices, Vol. 36, pp. 1929-1933, 1989.

[13]   T. Noguchi, "Appearance of single-crystalline properties in fin-patterned Si TFTs by solid phase crystallization," Jpn. J. Appl. Phys., pt. 2, Vol. 32, No. 11A, pp. 1584-1587, 1993.

[14] S.-W. Lee and S.-K. Joo. "Low temperature poly-Si thin film transistor fabrication by metal-induced lateral crystallization," IEEE Electron Device Lett., Vol. 17, pp. 160-162, 1996.

[15]   N. Kuno, N. Kusumoyo, T. Insushima, and S. Ymaazaki, "Characterization of polycrystalline-Si thin-film transistor fabricated by excimer laser annealing

method," IEEE Trans. Electron Devices, Vol. 40, pp. 1876-1879, 1994.

[16]   A.T. Voutsas, M.K. Hatalis, "Structure of As-Deposited LPCVD Silicon Films at Low Deposition Temperatures and Pressures".J. Electrochem, Soc. 139 (1992) 2659.

[17]   A.T. Voutsas, M.K. Hatalis, "DEPOSITION AND CRYSTALLIZATINO OF A-SI LOW-PRESSURE CHEMICALLY VAPOR-DEPOSITED FILMS OBTAINED BY LOW-TEMPERATURE PYROLYSIS OF DISILANE"., J. Electrochem, Soc. 140(1993) 871

[18]   A.T.Voutsas,M.K. Hatalis, "STRUCTURAL CHARACTERISTICS OF AS-DEPOSITED AND CRYSTALLIZED MIXED-PHASE SILICON FILMS"., J. Electrochem, Soc. 23 (1994) 319.

[19]   Miyasaka M, Shimoda T, Makihira K, Asano T, Pecz B, Stoemenos, "Structural Properties of Nickel Metal-Induced Laterally Crystallized Silicon Films and Their Improvement Using Excimer Laser Annealing", Jpn.J.Appl.Phys. Vol. 42 (2003) 2592

[20]   Naoyuki Higashi, Gou Nakagawa, Tanemasa Asano,Mitsutoshi Mitasaka, John Stoemenos, "Location and Orientation Control of Si Grain by Combining Metal-Induced Laterally Crystallized Silicon and Excimer Laser Annealing", Jpn.J.Appl.Phys. Vol. 45 (2006) 4347.

[21]   Toshiyuki SAMESHIMA and Nobuyuki ANDOH, "Heating Layer of Diamond-Like Carbon Films Used for Crystallization of Silicon Films", Japanese Journal of Applied Physics. Vol. 44, No. 10, 2005, pp. 7305–7308

[22]   A . Poruba, " Optical absorption and light scattering in microcrystalline silicon films and solar cells",JAP, Vol.88,2000.

[23]   J. Robertson, Materials Science and Engineering R37,129(2001)

[24] Wen-Chang Yeh, Masakiyo Matsumura, "Proposed Sample Structure for Enlargement of Excimer-Laser-Induced Lateral Grain Growth in Si Thin Films",Jpn. J. Appl. Phys. Vol. 41 (2002) 1909 arked

[25] H. Makihara, A . Tabata, Y. Mizutani, "Effect of the hydrogen partial pressure ratio on the properties of μc-Si:H films prepare by rf magnetron sputtering ", Vacuum, 59, pp. 785-791(2000)

[26] Siebke F, Yata S, Hishikawa Y, Tanaka M. J Non-Cryst Solids 1998;227-230:977.

Table I Thermal conductivity, density, specific heat and other parameters used in the simulation. The value of absorption coefficient was measured by n&k analyzer.

	Si	SiO2	DLC
$\rho\,(g/\,cm^3)$	2.33	2.22	1.95
$c\,(J\,K^{-1}\,Kg^{-1})$	712	745	717
$k\,(W\,K^{-1}\,m^{-1})$	25	1.38	1.6
$\alpha\,(m^{-1})$	7×10^4	450	1.7×10^7
$L\,(J\,m^{-3})$	3×10^9	——	——
$T_m\,(^{\circ}C)$	1410	——	——

Table II The absorption coefficient of a-C:H film which deposits in different condition. The wave length of laser (a) $\lambda = 351$ nm   (b) $\lambda = 532$ nm

   (a)

	$k\,(W/m.K)$	$\alpha\,(cm-1)$	$A\,(cm^{-1})$
25%(CH4) 120m 100w	0.36255	147921.6	0.829920
50%(CH4) 30m 100w	0.42034	171501.3	0.798082
50%(CH4) 60m 50w	0.35169	143490.7	0.801809
75%(CH4) 30m 100w	0.39885	162730.6	0.823072
100%(CH4))30m 100w	0.37610	153451.9	0.836710

   (b)

	$k\,(W/mK)$	$\alpha\,(cm-1)$	$A\,(cm^{-1})$
25%(CH4) 120m 100w	0.203376	48039.49	0.532799
50%(CH4) 30m 100w	0.234059	55286.97	0.479878
50%(CH4) 60m 50w	0.175084	41356.59	0.459495
75%(CH4) 30m 100w	0.227748	53796.44	0.534881
100%(CH4))30m 100w	0.226210	53433.15	0.578374

Table Ⅲ (a) The I(G)/I(D) of a-C:H film before and after laser irradiated (b) Thermal conductivity, density, and other heat capacity of sp^2-band and sp^3- band.

(a)

	I(G)/I(D)
without laser	1.645
100mJ/cm²	1.681
200mJ/cm²	1.392
300mJ/cm²	1.378
400mJ/cm²	1.108

(b)

	K (thermal conductivity)	ρ (density)	Cp (heat capacity)
SP²	1.6 (W/m.K)	1.95 (g/cm²)	717 (J/Kg.K)
SP³	200~2000 (W/m.K)	3.51 (g/cm²)	516 (J/Kg.K)

Table Ⅳ The Xc(crystalline volume factor) of (a) sample A and (b) sample B with different laser energy density

(a)

Laser energy (mJ/cm²)	Xc(%)
175	85.5
200	86.5
250	89.8
275	90.5

(b)

Laser energy (mJ/cm²)	Xc(%)
175	82.1
200	82.9
250	83.6
275	84.4

Chapter 1
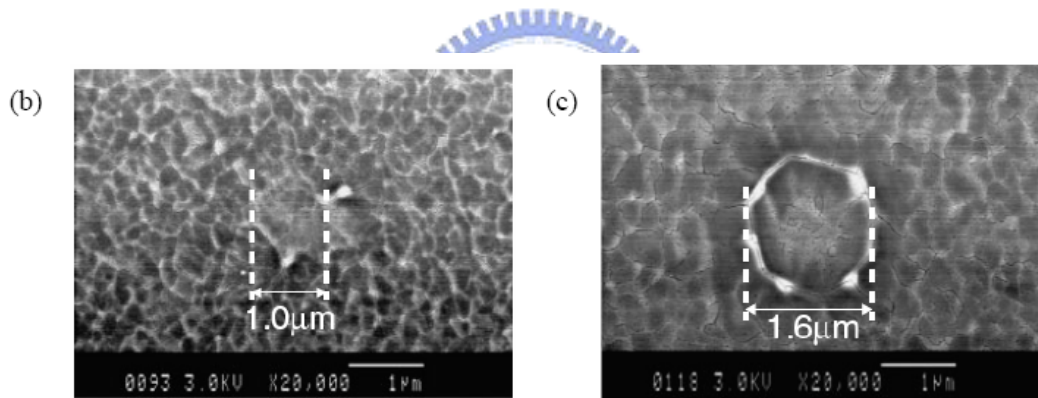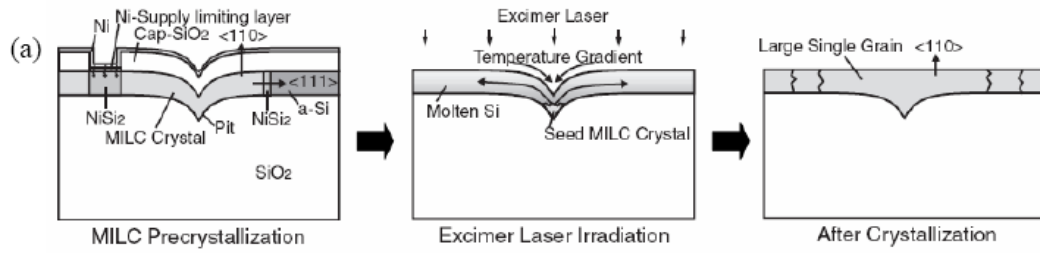
Fig. 1-1-1 (a) fabrication procedure combining MILC and ELA with a pitstructure (b) SEM image with laser energy = 733mJ/cm^2 (c) SEM image with laser energy = 775 mJ/cm^2.

(a)

(b)

(c)
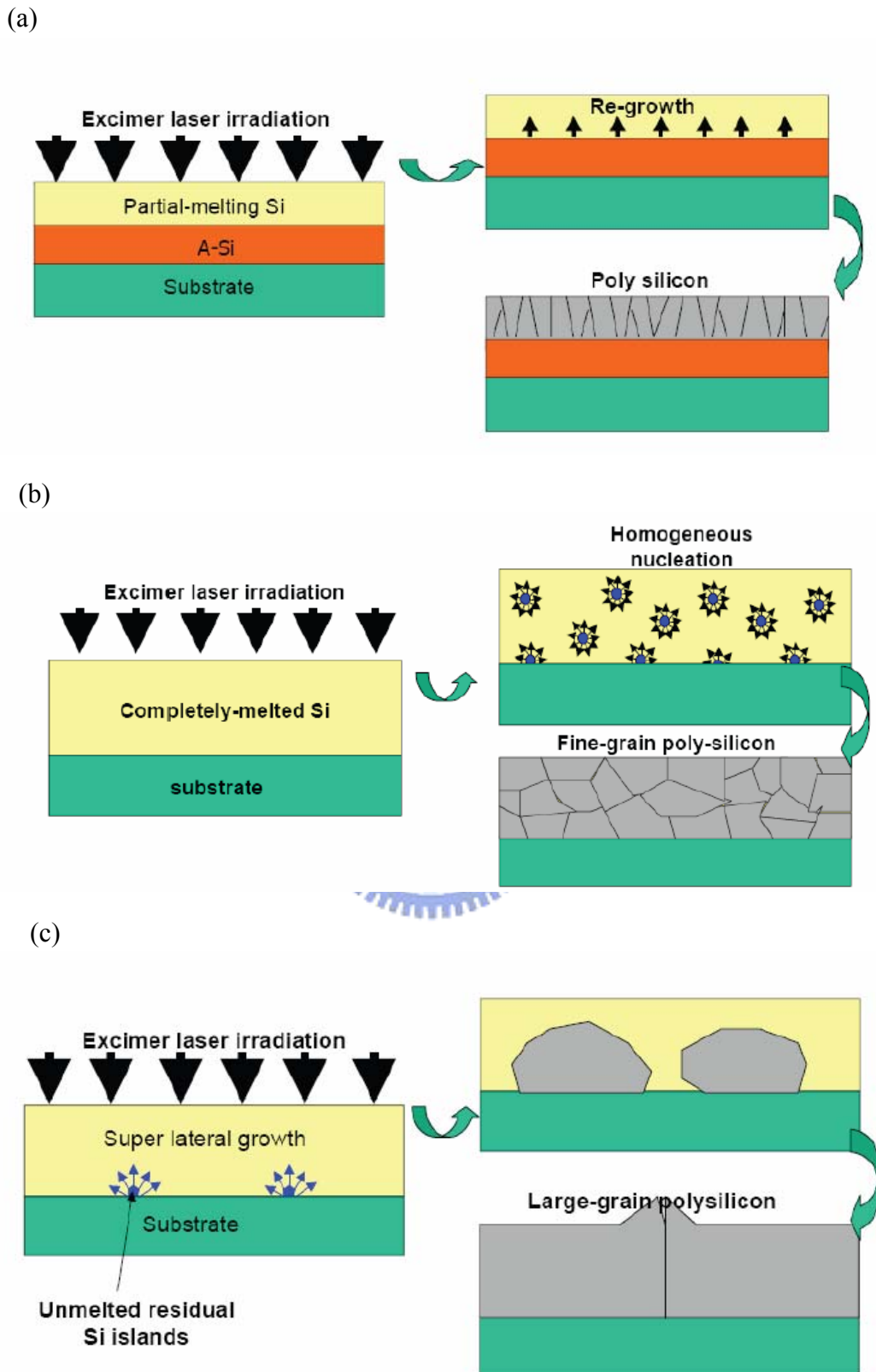
Fig.1-1-2   According to the laser energy density, the crystallization could be discussed into three regimes: (a) partially melting fluence, (b) completely melting fluence, (c) super lateral growth (SLG).
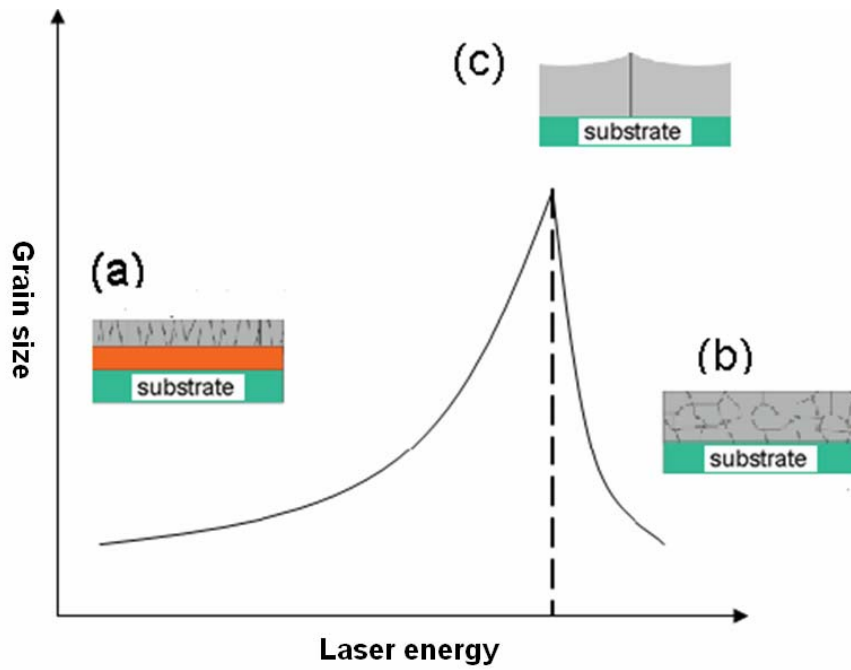
Fig.1-1-3 The relation between the laser fluence and the grain size.
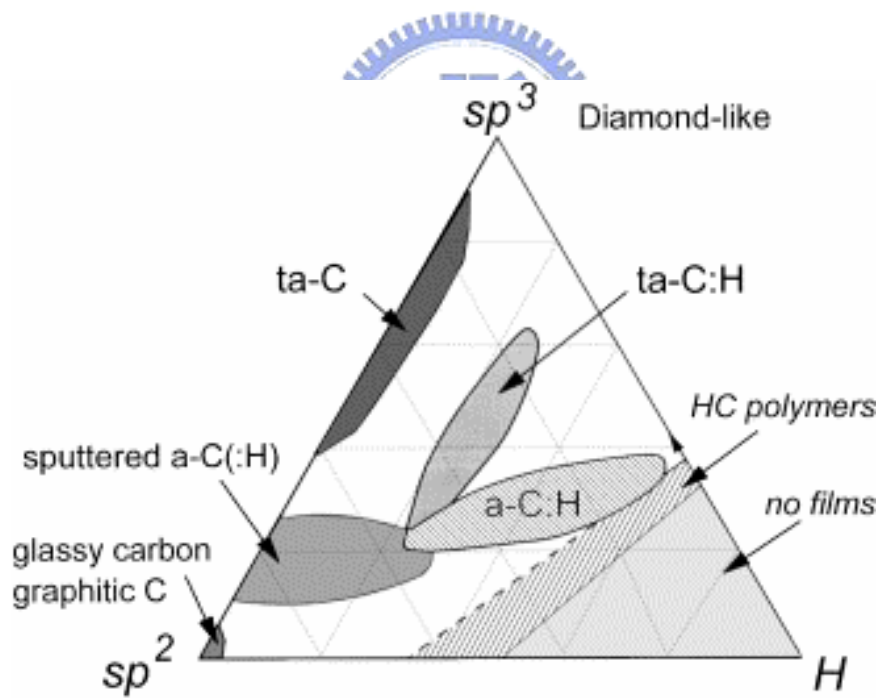
Fig.1-2-1 Ternary phase diagram of bonding in amorphous carbon–hydrogen alloys.

Chapter 2
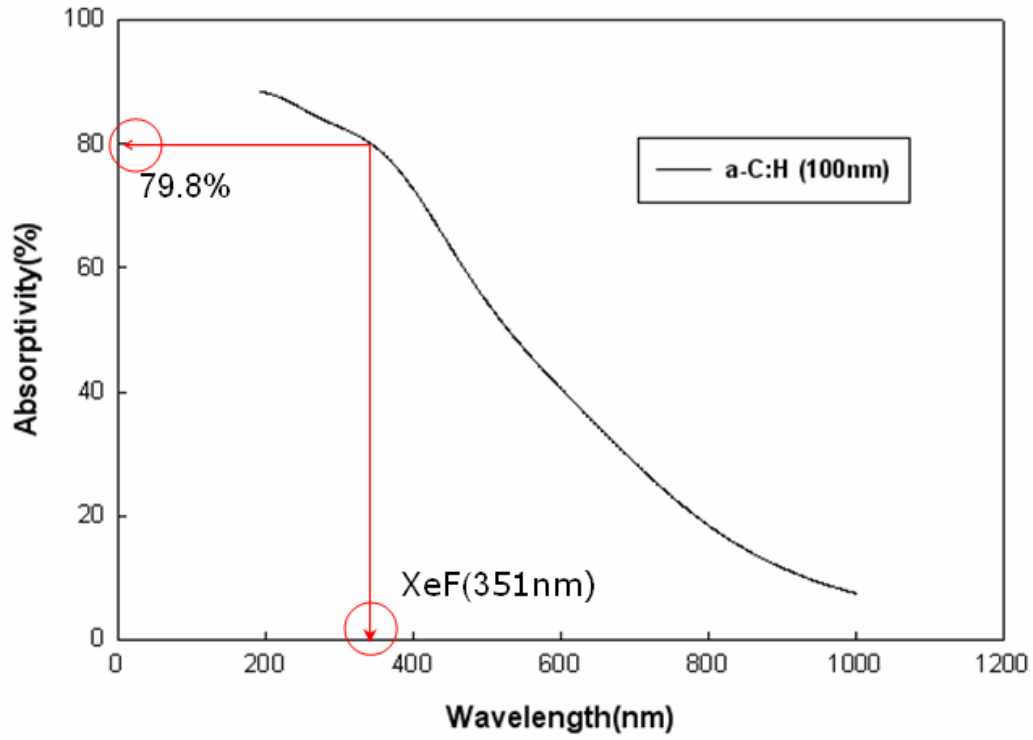
Fig. 2-2-1 The absorptivity of a-C:H film. The thickness of a-C:H is 100nm.
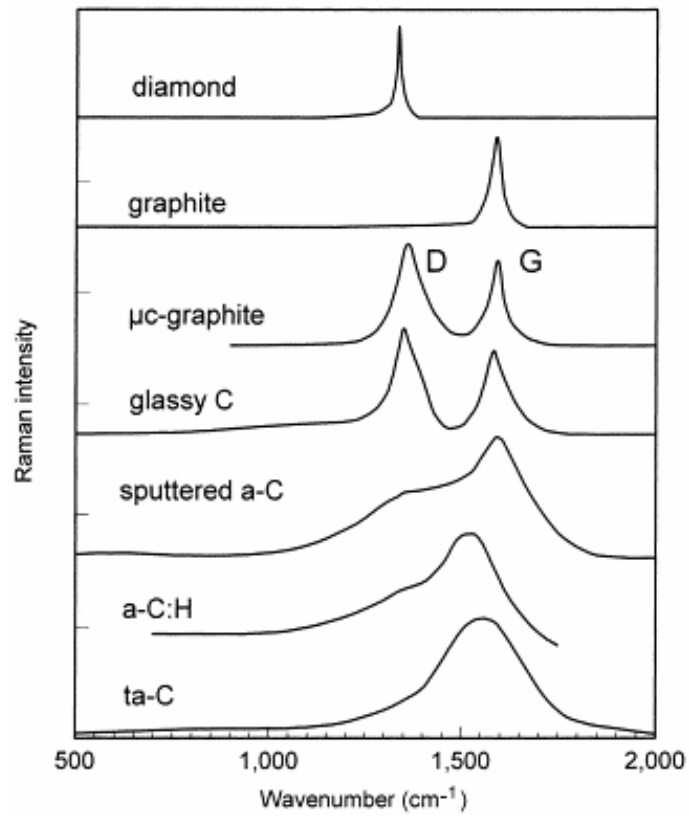
Fig. 2-2-2 The Raman spectra of the carbon film
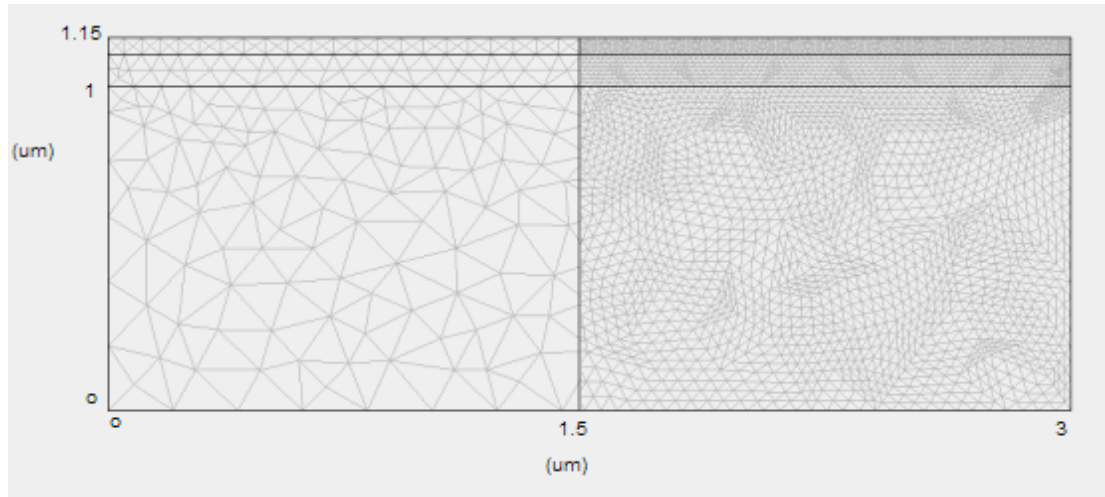
Fig. 2-3-1 The left part of picture is the normal meshes in the structure and the right part is the refined meshes in the structure. The refine meshes would increase the accuracy of the final result.
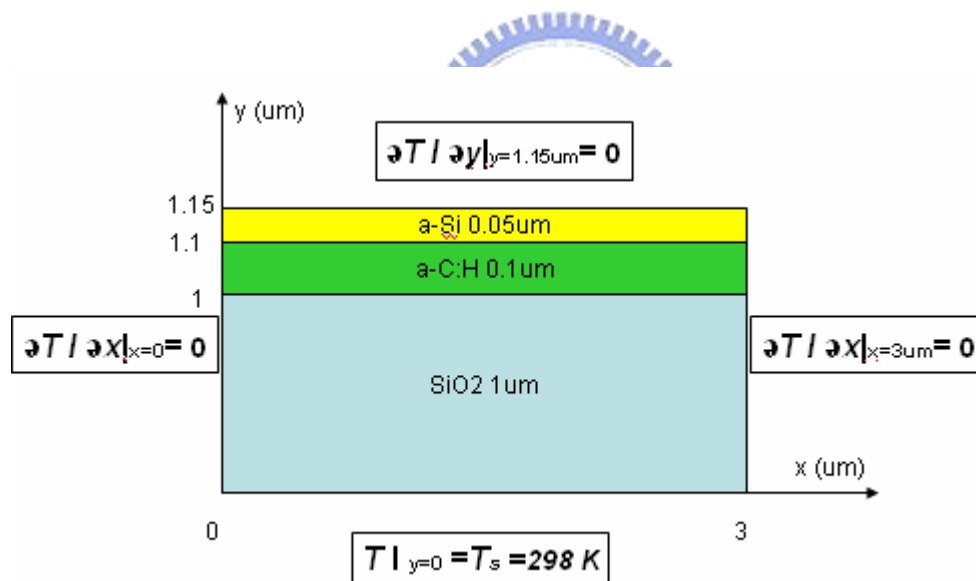
Fig. 2-3-2 The structure for simulation, the top layer is α-Si ,the middle lay is a-C:H ,and the bottom layer is SiO_2. The dimensions and the boundary conditions of each side are labeled on it.

(a)
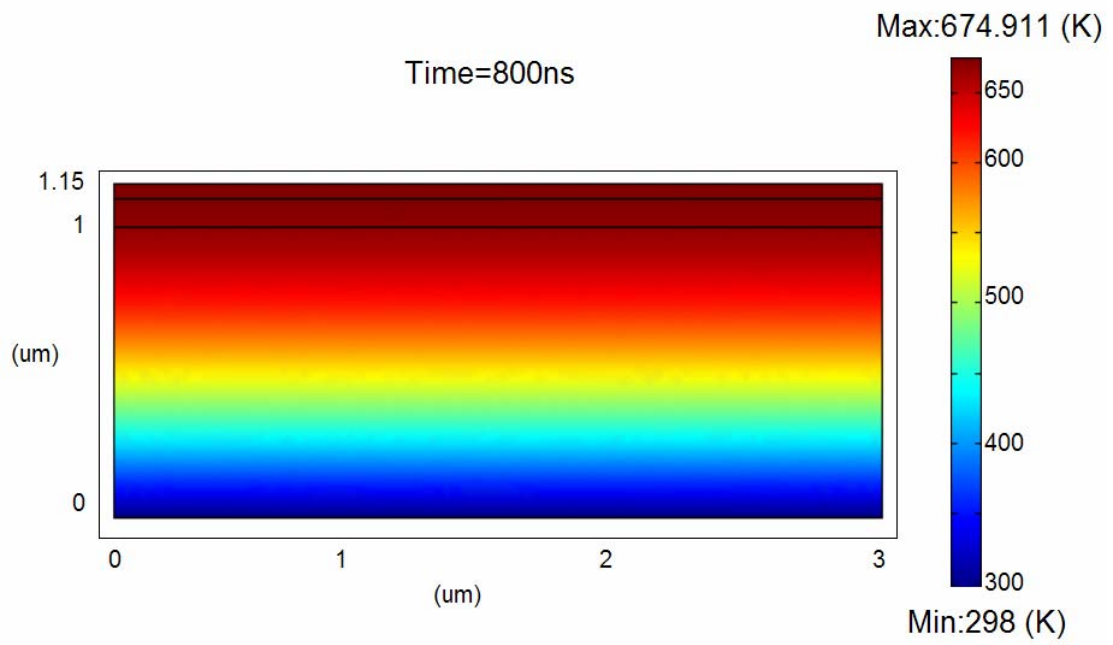
(b)
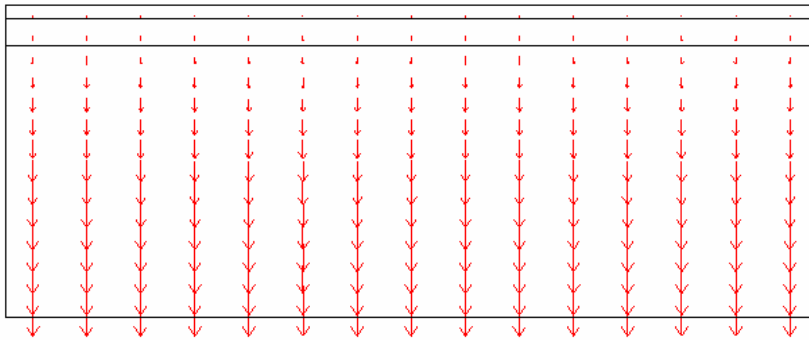
(c)
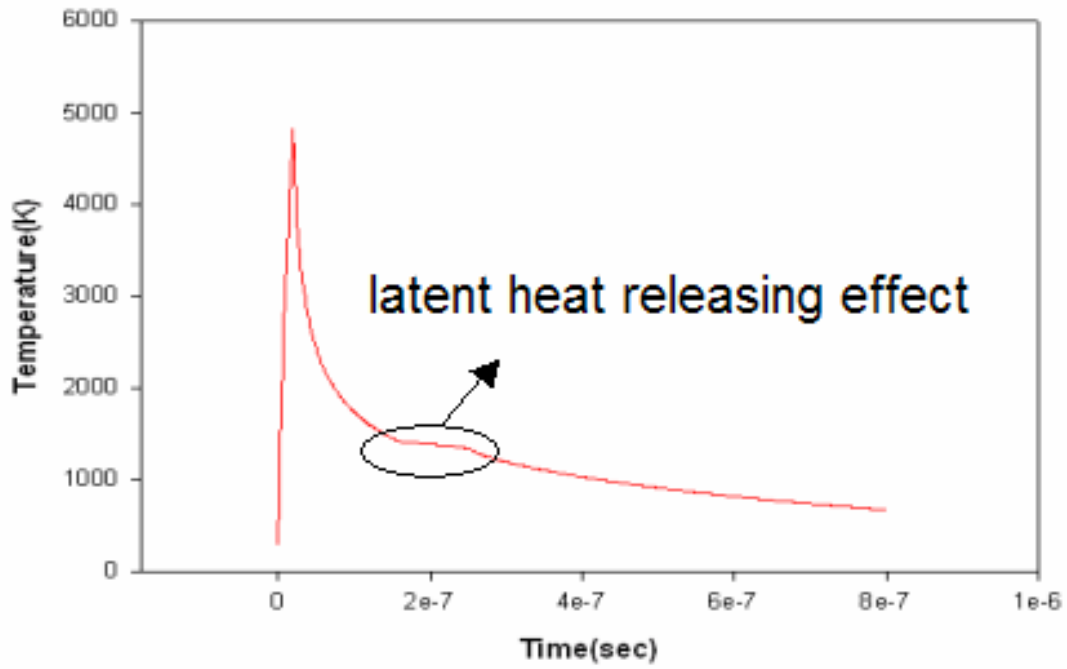
(d)
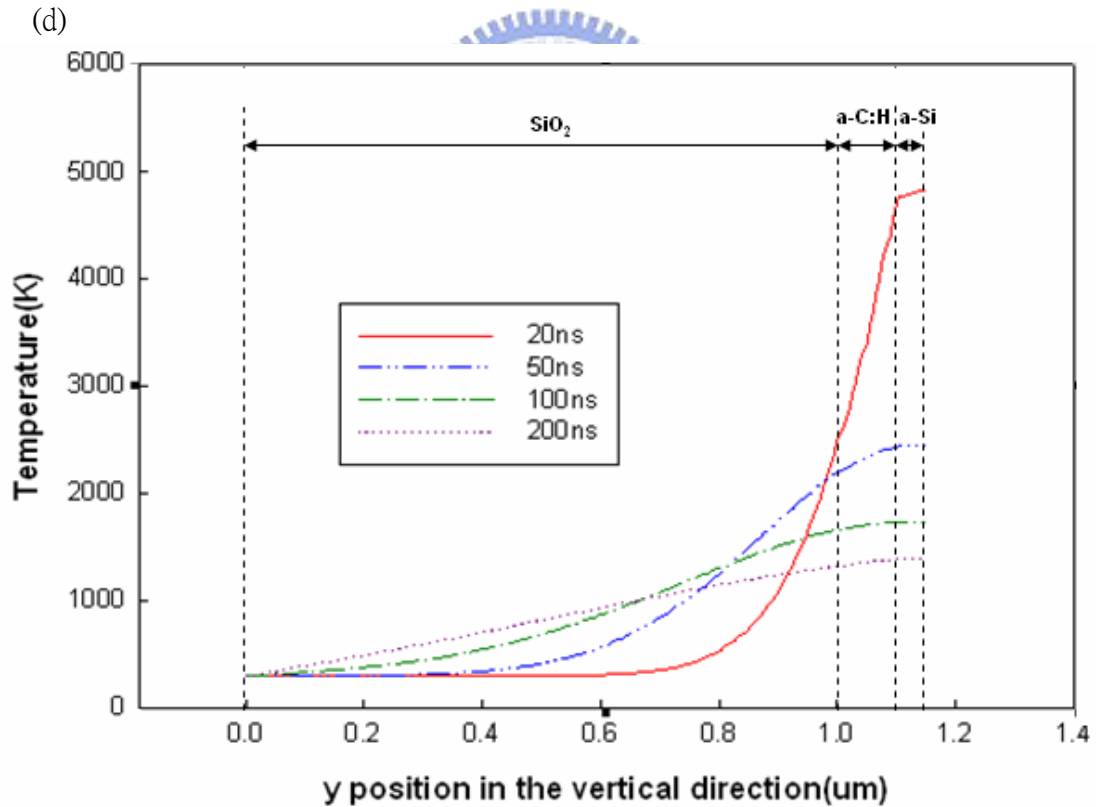
Fig. 2-3-3 (a) Thermal distribution at a certain time = 800 ns, (b) the contour lines of the heat flux at a certain time = 800ns (c) Temperature curve of a particular point (1.5μm, 1.15μm) versus the time (d) Temperature curve versus the position of y at different time (at 20ns, 50ns, 100ns, and 200ns)

Chapter 3

(a)

(b)

(c)
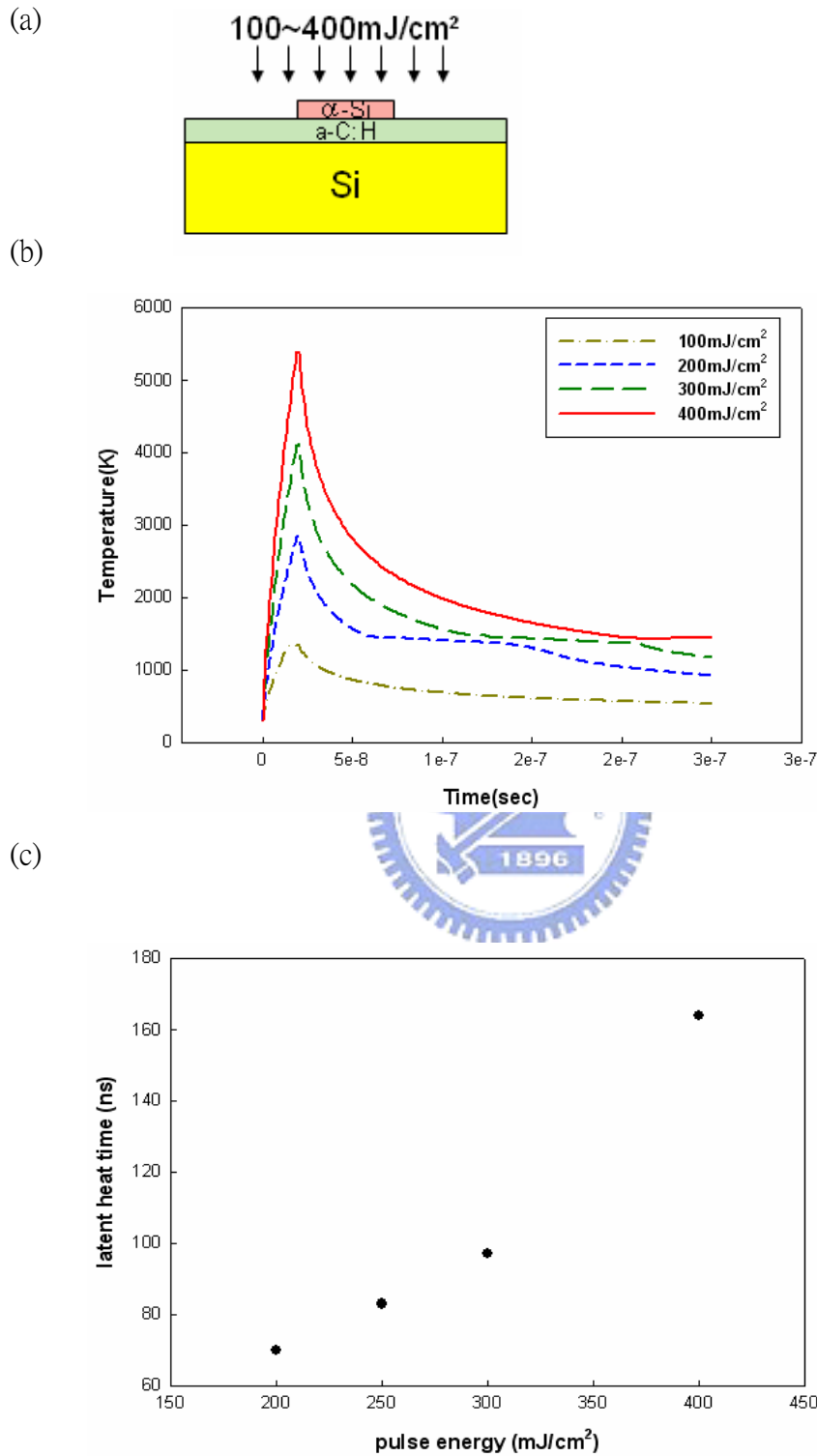
Fig. 3-1-1 (a) The cross section of the structure (b) The temperature curve versus the time with different laser energy (c) The latent heat time versus the laser energy

(a)

(b)
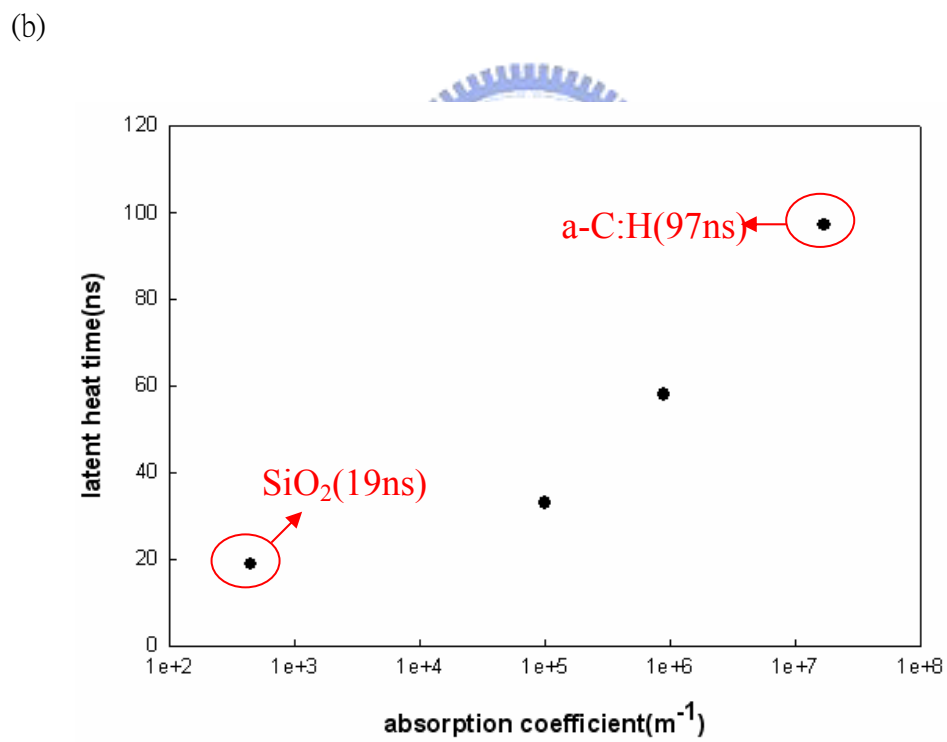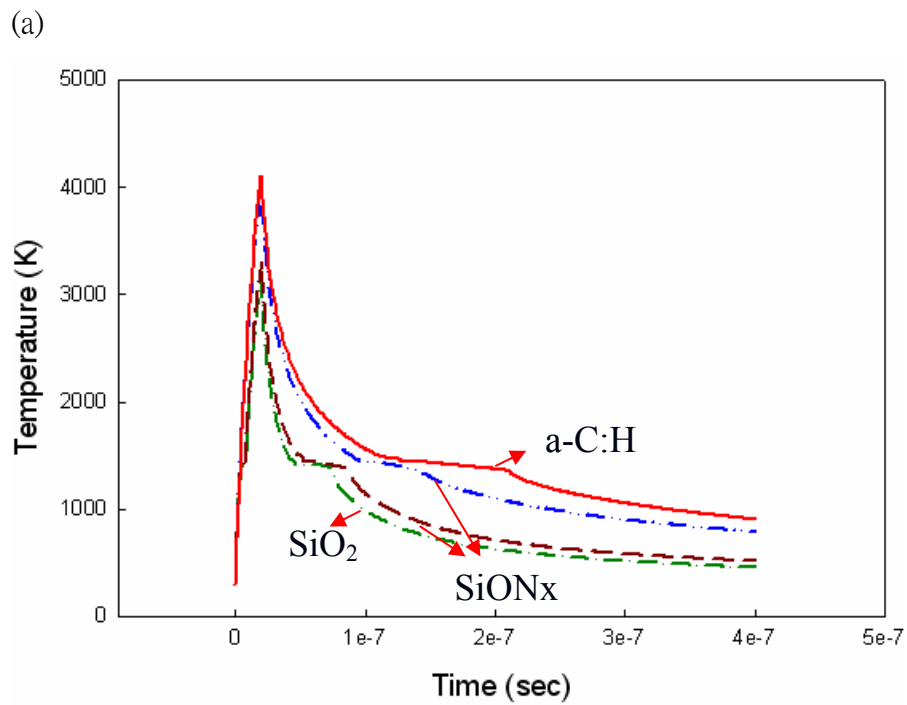
Fig. 3-1-2 (a) The temperature curve versus the time with different absorption coefficient (b) The latent heat time versus the absorption coefficient

(a)

(b)

(c)

(d)
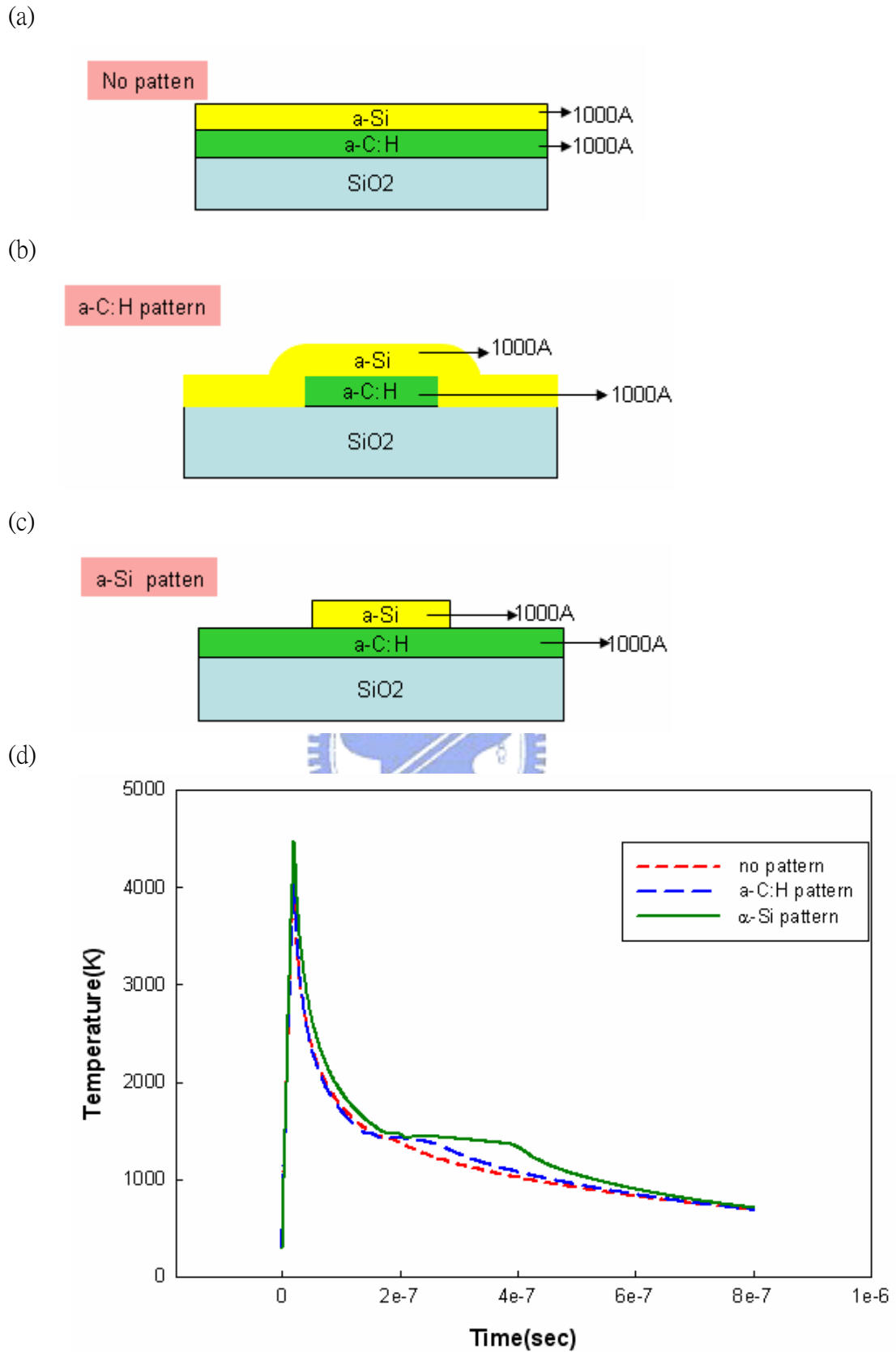
Fig. 3-1-3 (a) The a-C:H film deposit on the SiO2,and then the a-Si deposit on a-C:H film without pattern. (b) a-C:H with pattern (c) a-Si with pattern (d) The temperature curve versus the time with different Structures.
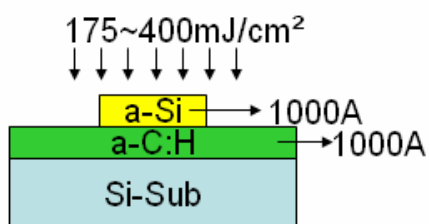
(a)   (b)
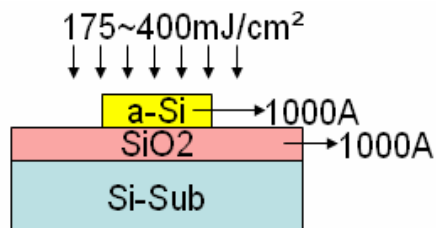
Fig. 3-1-4 (a) The cross-section of sample A   (b) The cross-section of sample B
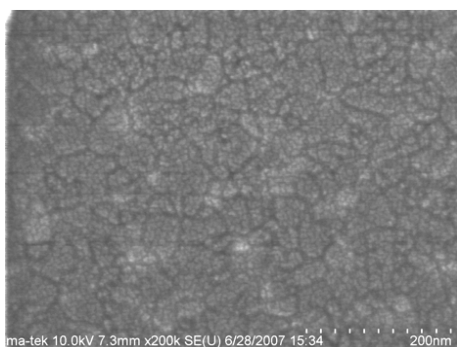
(a)   (b)
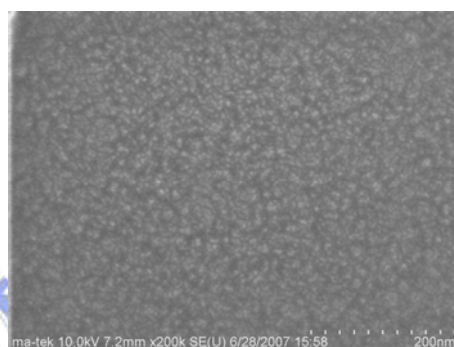
Fig. 3-1-5 (a) SEM image of sample A   Fig. 3-1-5 (b) SEM image of sample B
with laser energy density of 175 mJ/cm^2 with laser energy density of 175 mJ/cm^2
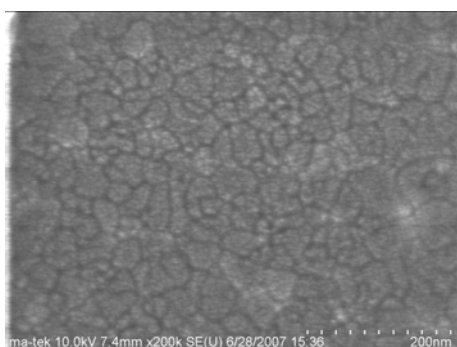
(c)   (d)
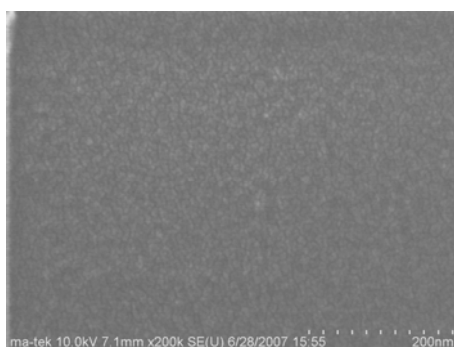
Fig. 3-1-5 (c) SEM image of sample A   Fig. 3-1-5 (d) SEM image of sample B
with laser energy density of 200 mJ/cm^2 with laser energy density of 200 mJ/cm^2

(e)

(f)
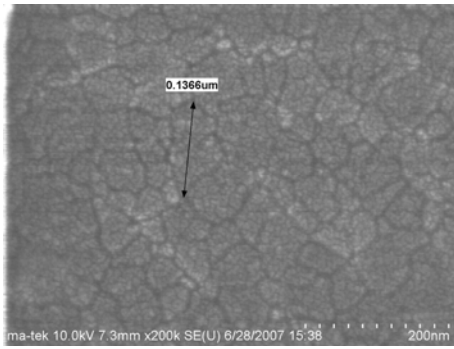
Fig. 3-1-5 (e) SEM image of sample A
with laser energy density of 225 mJ/cm^2
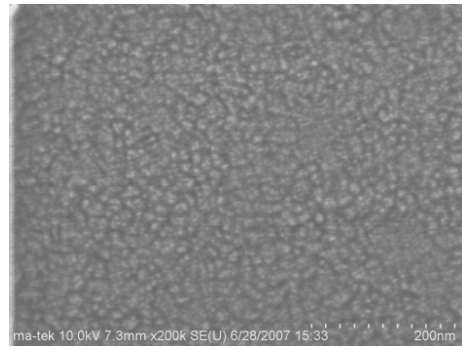
Fig. 3-1-5 (f) SEM image of sample B
with laser energy density of 225 mJ/cm^2

(g)

(h)
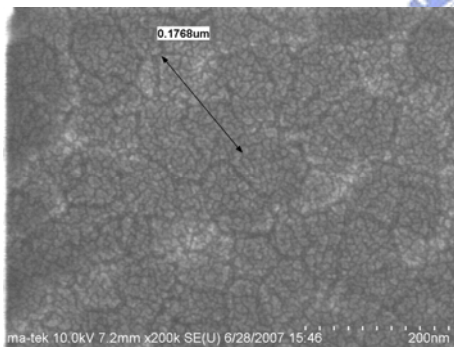
Fig. 3-1-5 (g) SEM image of sample A
with laser energy density of 250 mJ/cm^2
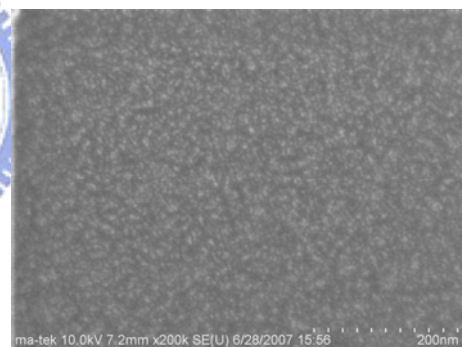
Fig. 3-1-5 (h) SEM image of sample B
with laser energy density of 250 mJ/cm^2

(i)   (j)
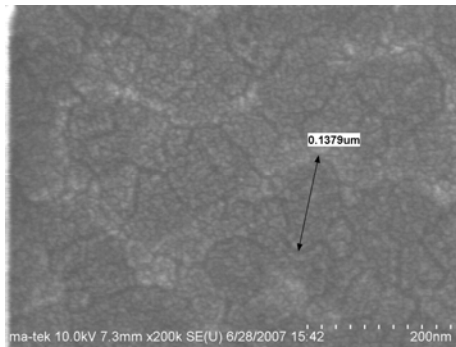
Fig. 3-1-5 (i) SEM image of sample A   Fig. 3-1-5 (j) SEM image of sample B
with laser energy density of 275 mJ/cm^2 with laser energy density of 275 mJ/cm^2
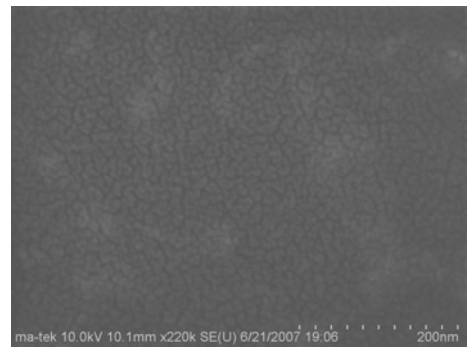
(k)   (l)
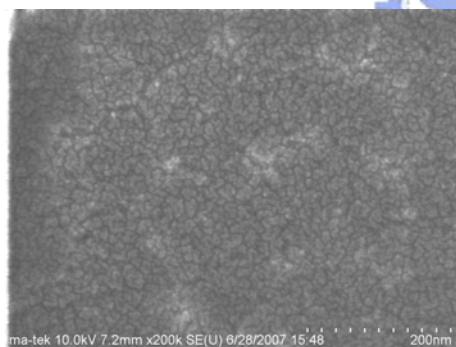
Fig. 3-1-5 (k) SEM image of sample A   Fig. 3-1-5 (l) SEM image of sample B
with laser energy density of 300 mJ/cm^2 with laser energy density of 300 mJ/cm^2
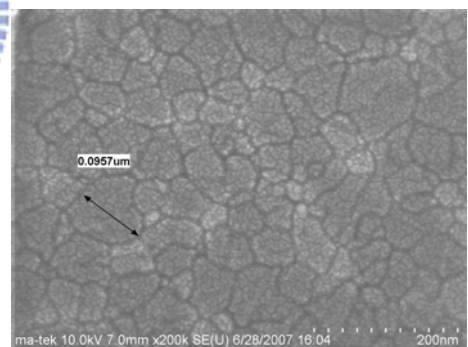
(m)   (n)
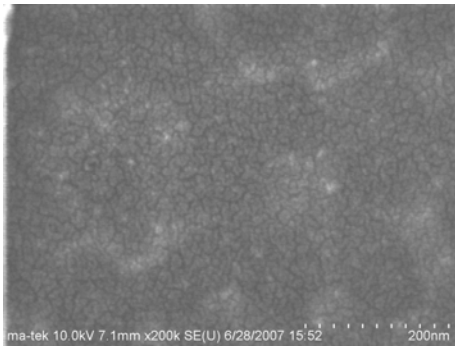
Fig. 3-1-5 (m) SEM image of sample A   Fig. 3-1-5 (n) SEM image of sample B
with laser energy density of 350 mJ/cm^2 with laser energy density of 350 mJ/cm^2
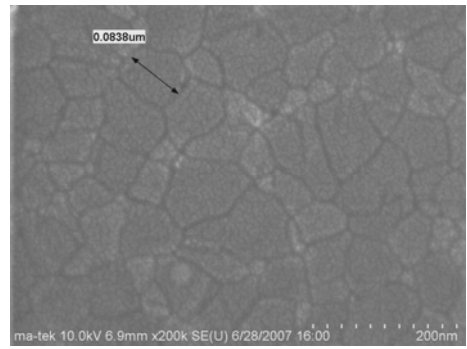
(o)   (p)
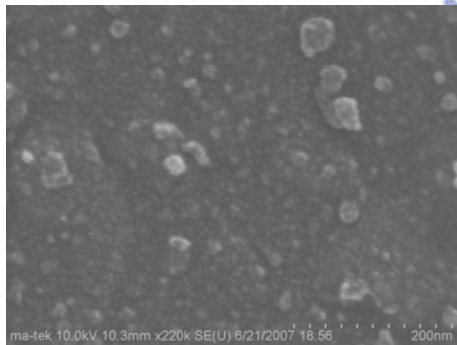
Fig. 3-1-5 (o) SEM image of sample A   Fig. 3-1-5 (p) SEM image of sample B
with laser energy density of 400 mJ/cm^2 with laser energy density of 400 mJ/cm^2
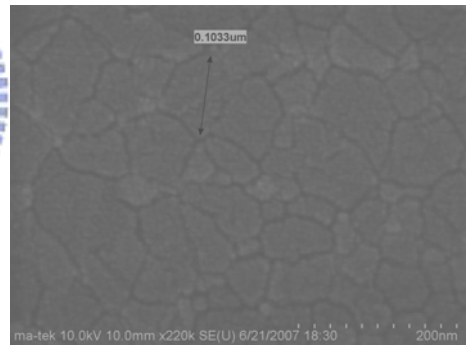
(a)
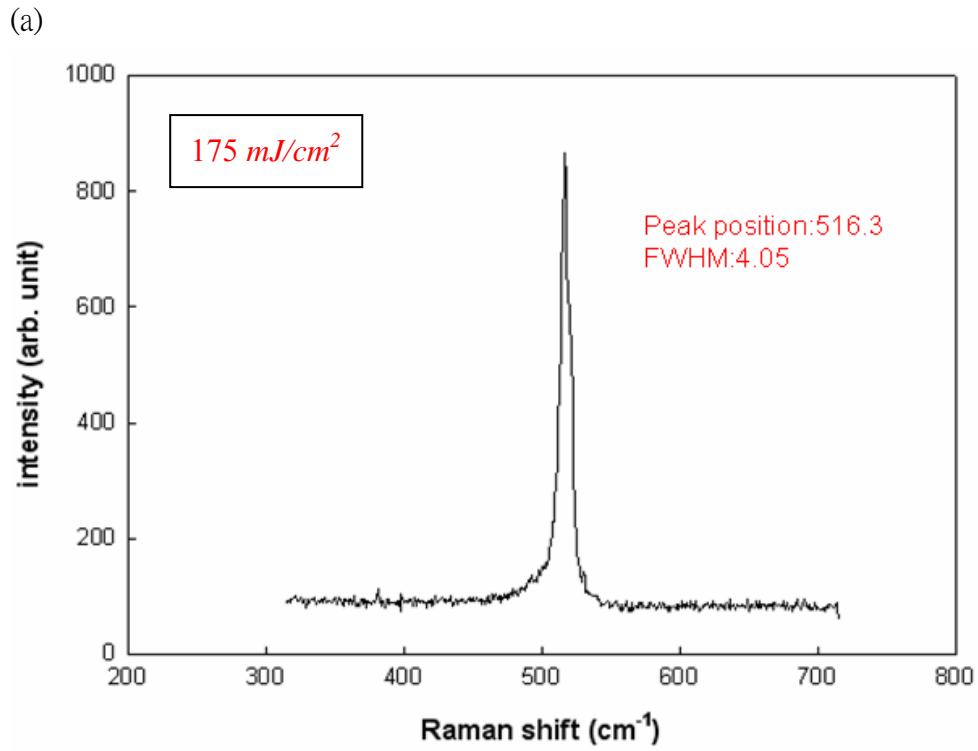
Fig. 3-2-1 (a) The Raman spectra of sample A with laser energy density of 175 mJ/cm^2

(b)
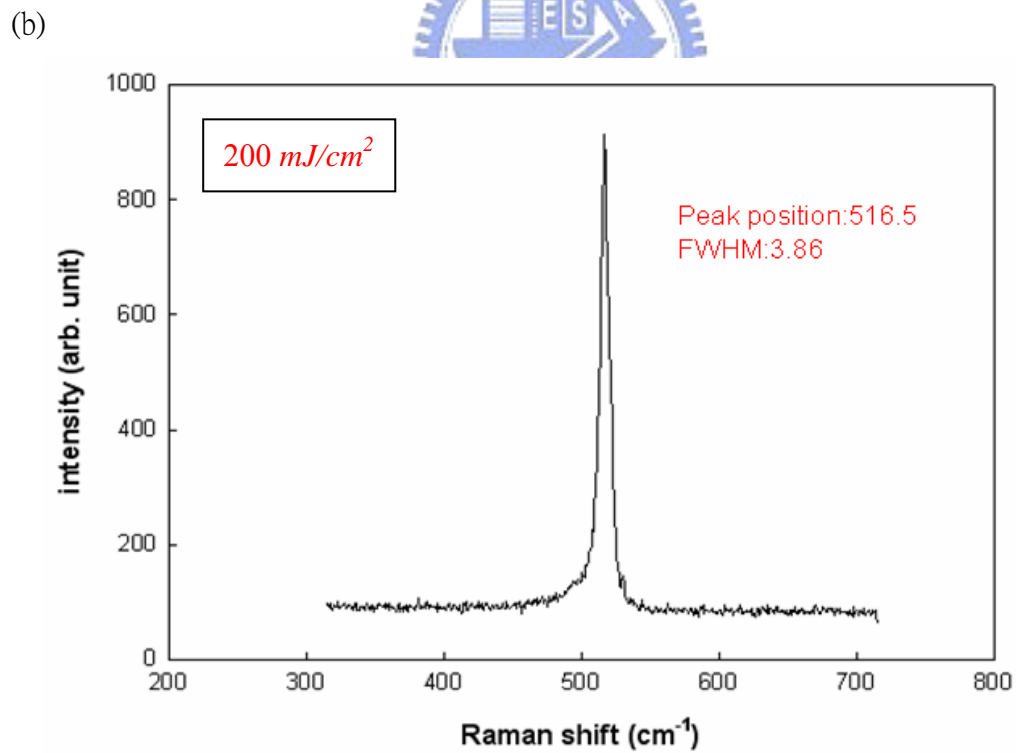
Fig. 3-2-1 (b) The Raman spectra of sample A with laser energy density of 200mJ/cm^2

(c)
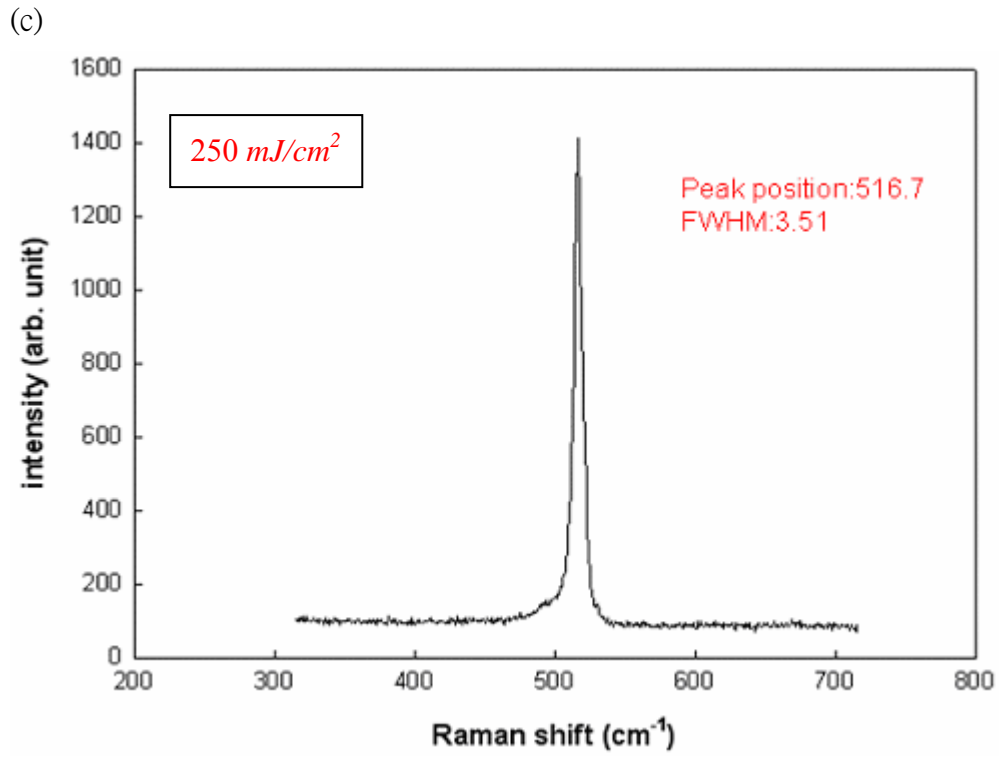
Fig.3-2-1 (c)The Raman spectra of sample A with laser energy density of 250mJ/cm^2
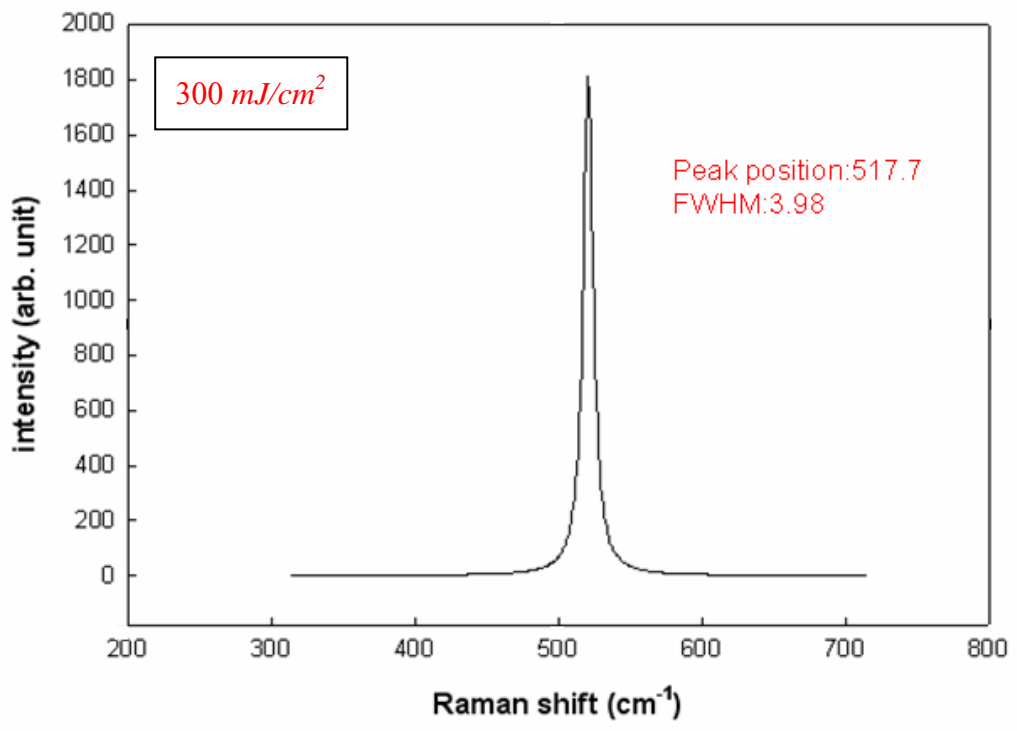
(d)
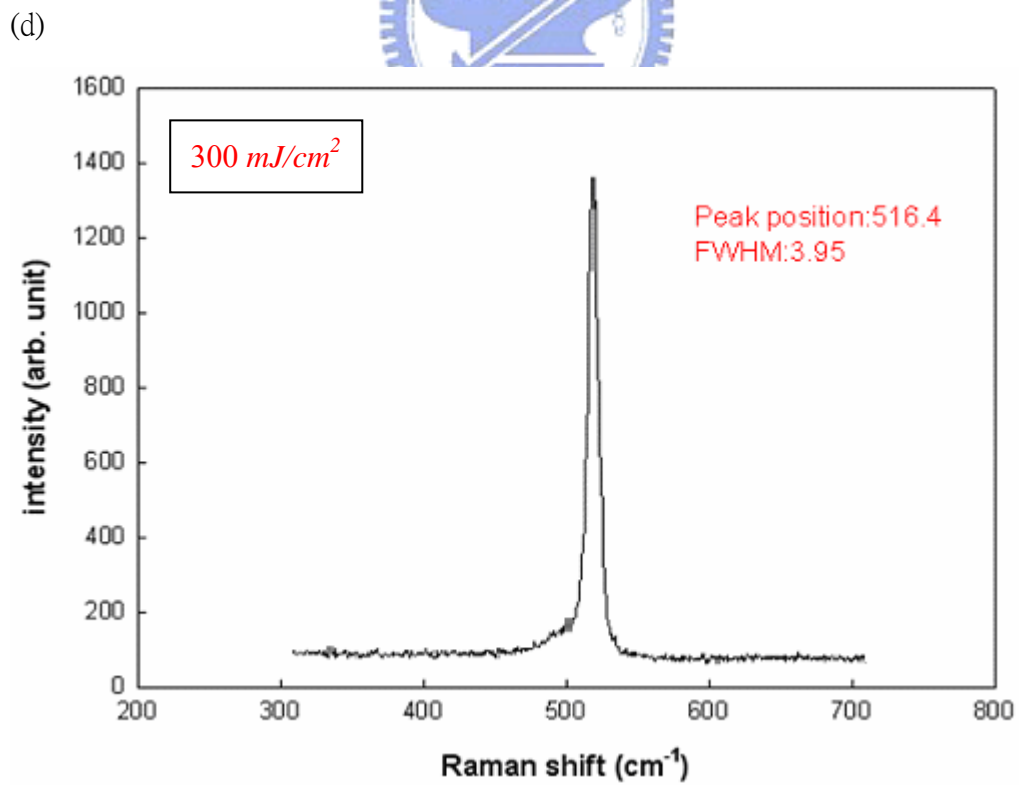
Fig. 3-2-1 (d) The Raman spectra of sample A with laser energy density of 300mJ/cm^2
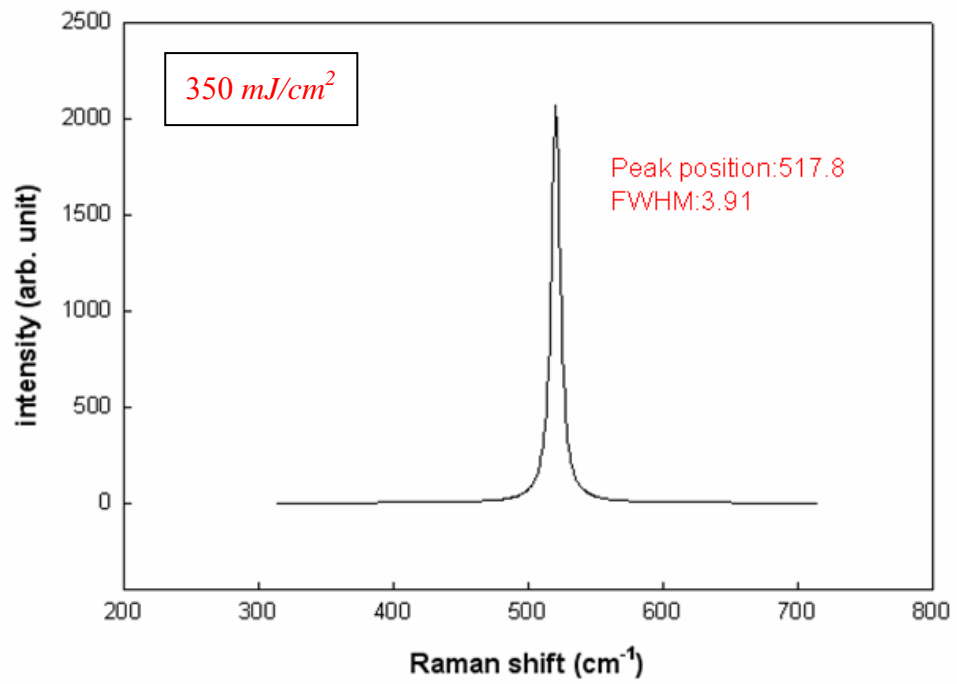
(e)
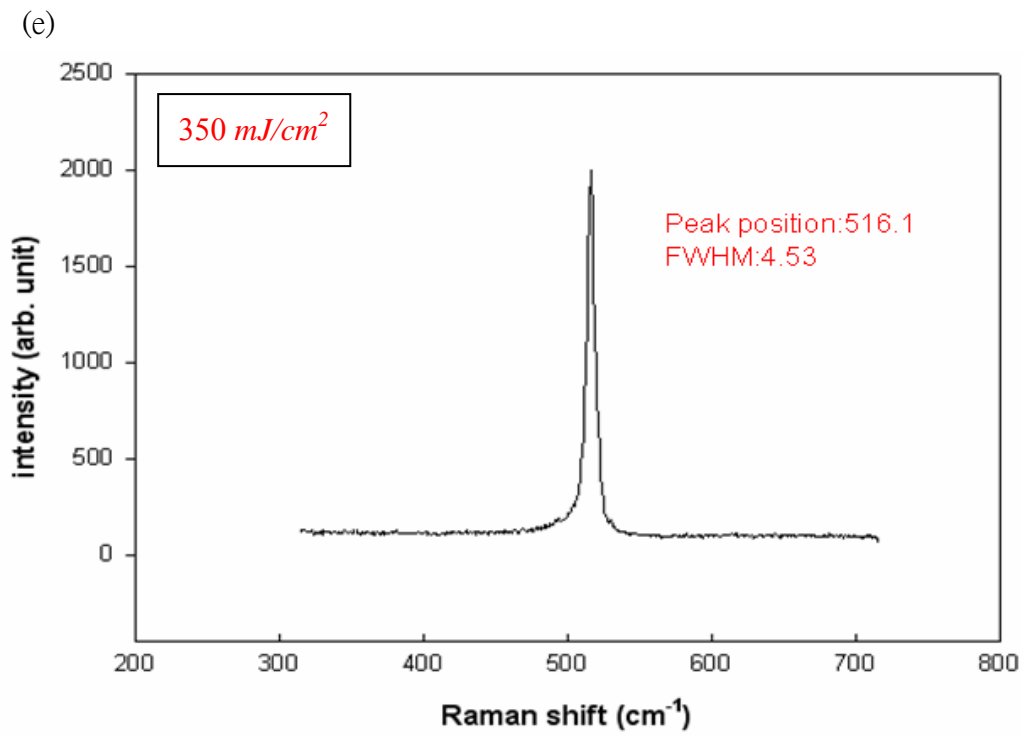
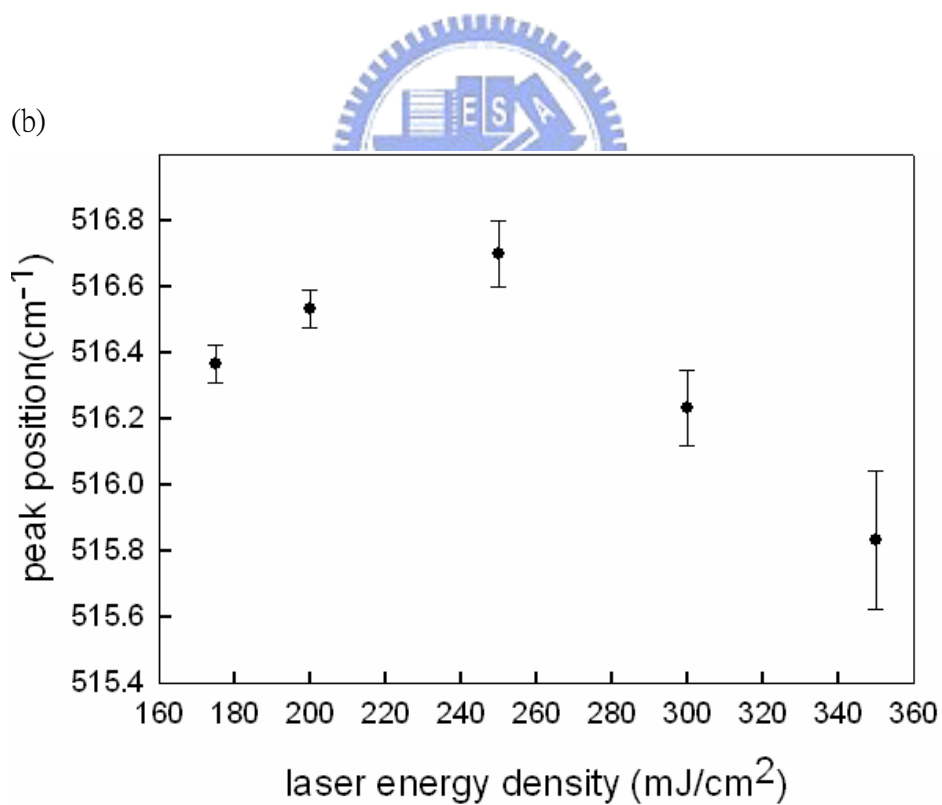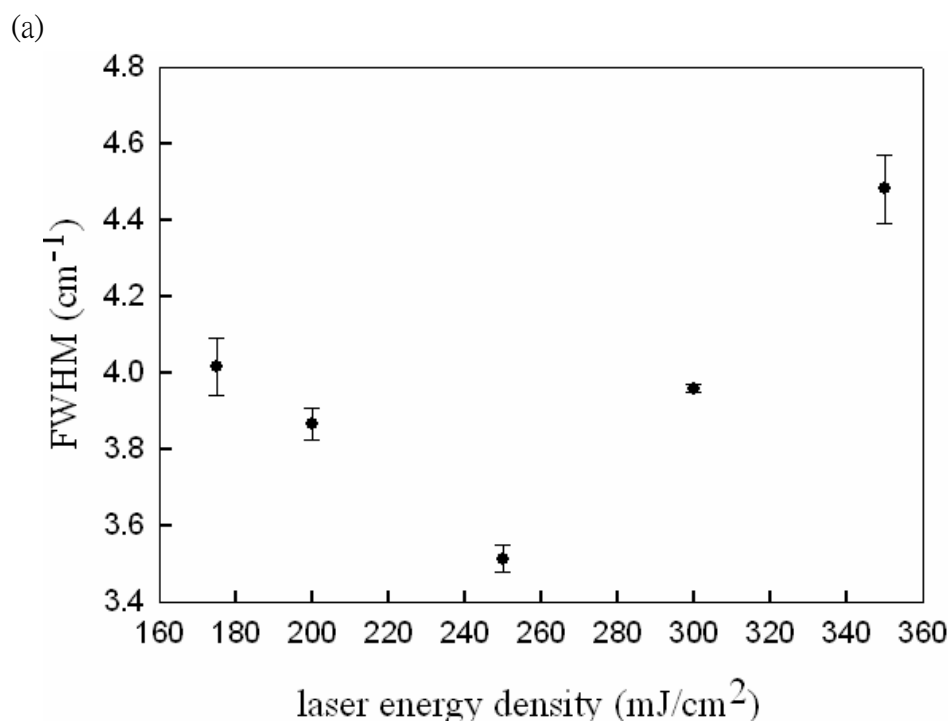Fig. 3-2-1 (e) The Raman spectra of sample A with laser energy density of $350mJ/cm^2$

(a)
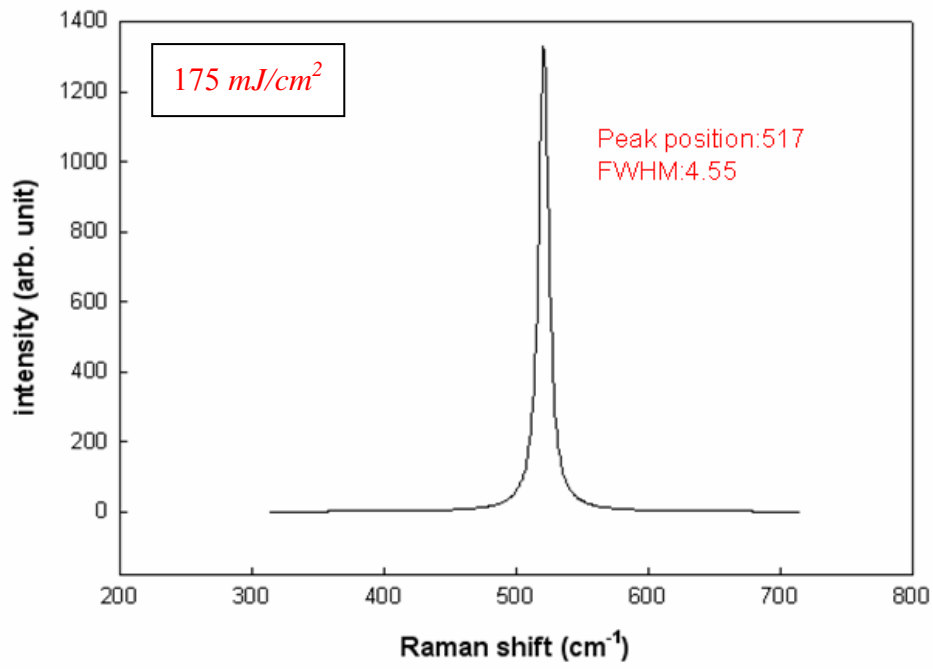
Fig. 3-2-2 (a) The Raman spectra of sample B with laser energy density of 175mJ/cm^2

(b)
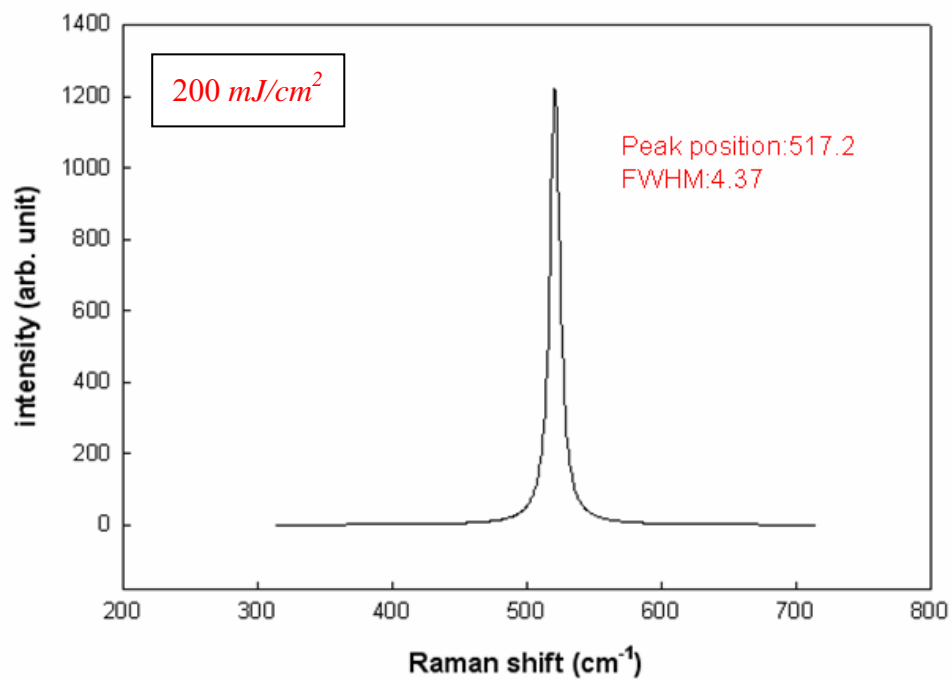
Fig. 3-2-2 (b) The Raman spectra of sample B with laser energy density of 200mJ/cm^2

(c)
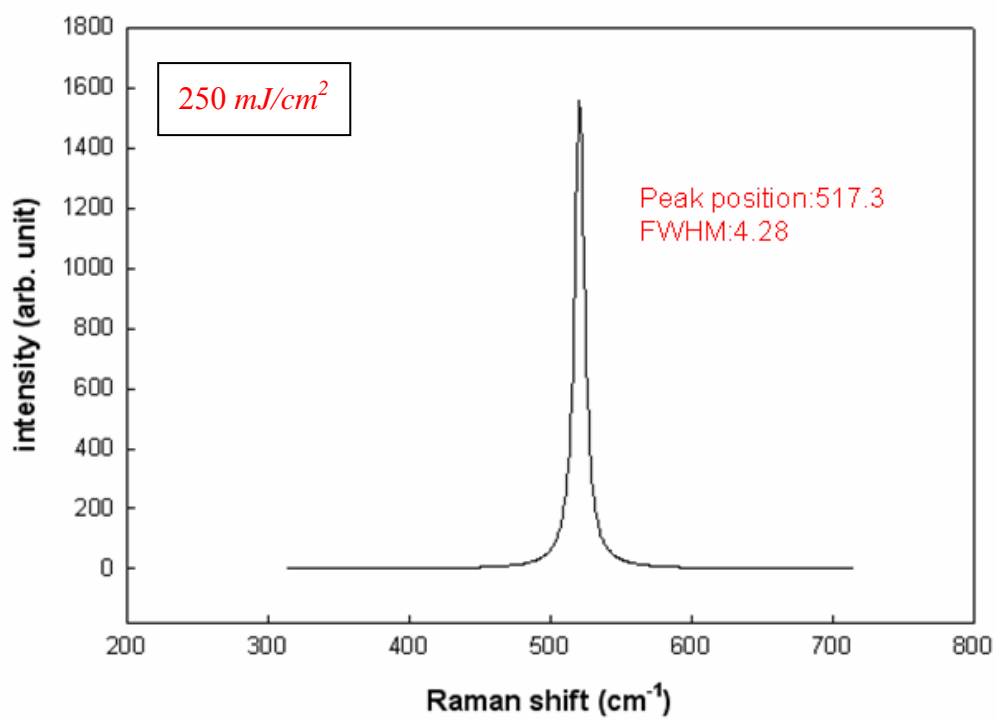
Fig. 3-2-2 (c) The Raman spectra of sample B with laser energy density of 250*mJ/cm²*

(d)

Fig. 3-2-2 (d) The Raman spectra of sample B with laser energy density of 300*mJ/cm²*

(e)

Fig. 3-2-2 (e) The Raman spectra of sample B with laser energy density of $350mJ/cm^2$
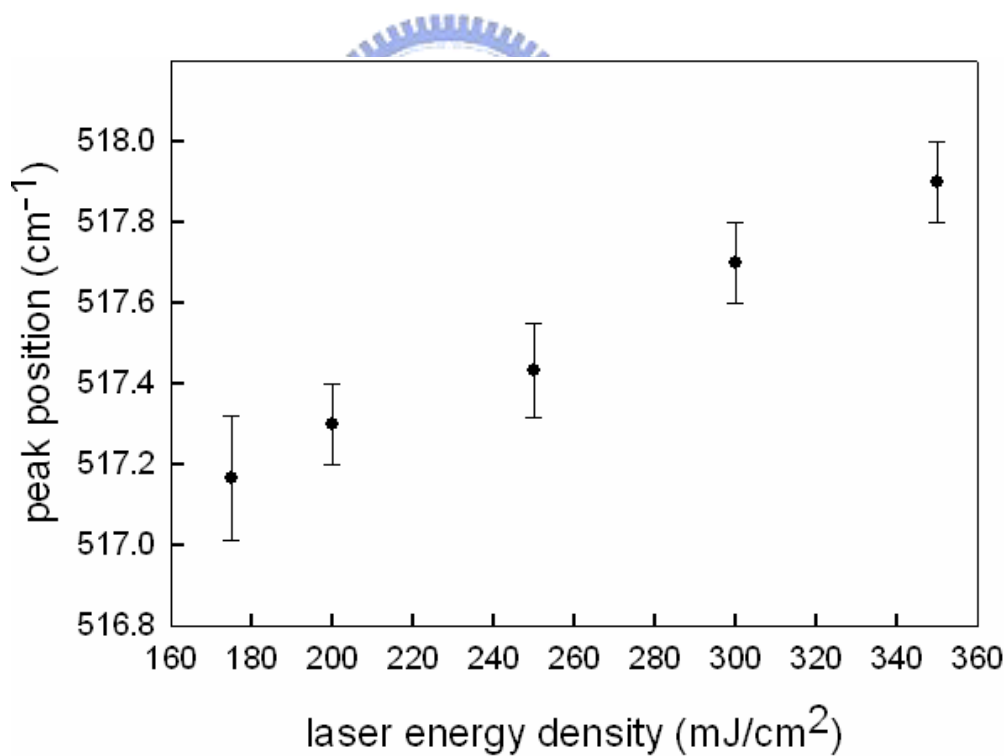
(a)

(b)

Fig. 3-2-3 (a) FWHM of sample A with laser energy density of 175 *mJ/cm²* ~ 350
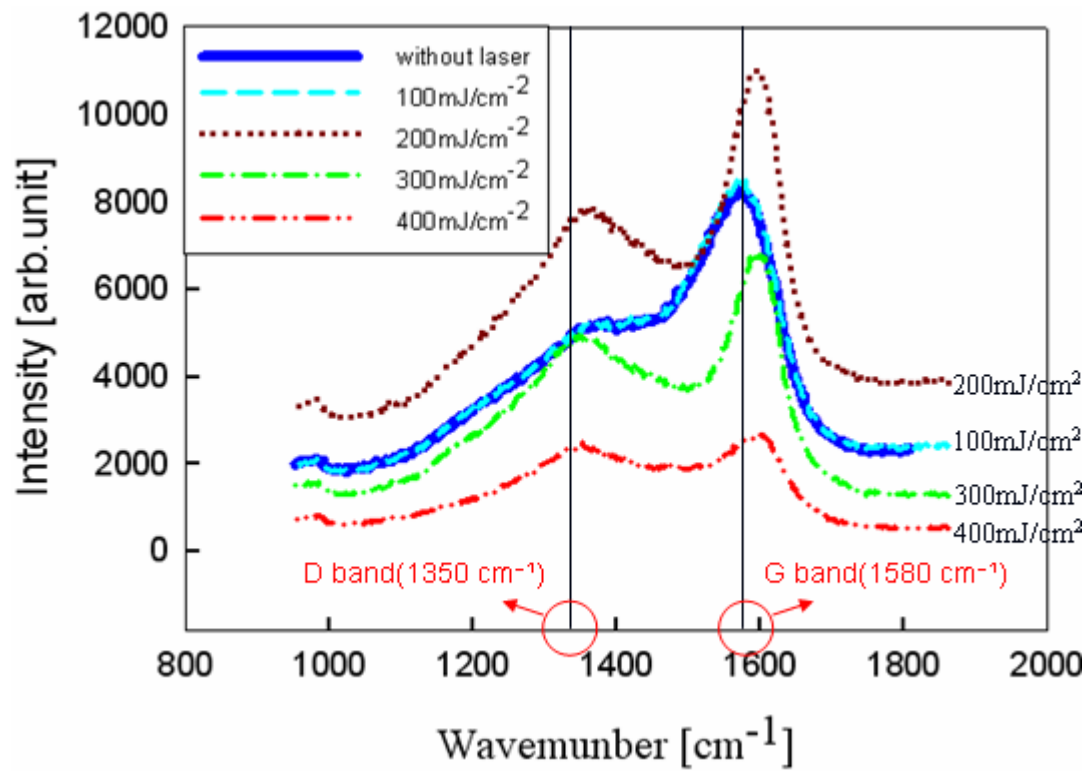*mJ/cm²* (b) peak position of sample A with laser energy density of 175 *mJ/cm²* ~ 350
mJ/cm²

(a)
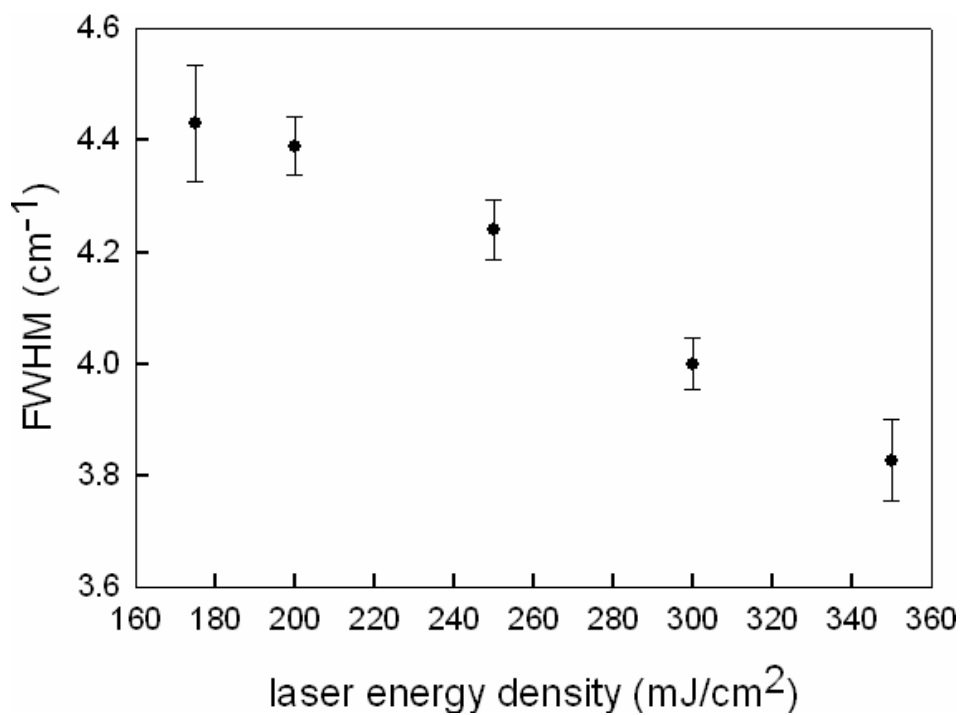
(b)

Fig. 3-2-4 (a) FWHM of sample B with laser energy density of 175 $mJ/cm^2 \sim 350$ mJ/cm^2 (b) peak position of sample B with laser energy density of 175 $mJ/cm^2 \sim 350$ mJ/cm^2

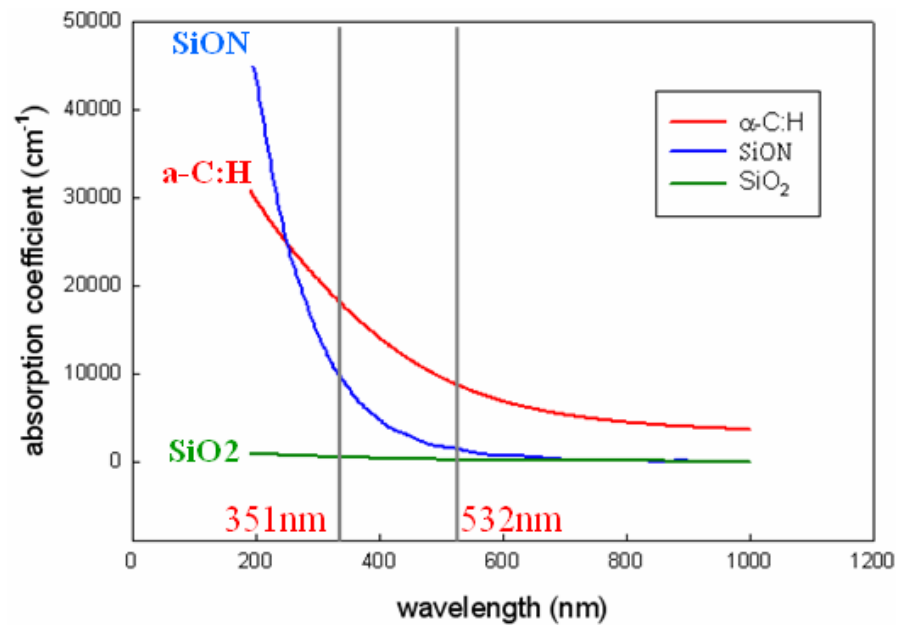Fig.3-2-5 The Raman spectrum of a-C:H before and after laser irradiated by 100 to 400*mJ/cm²*

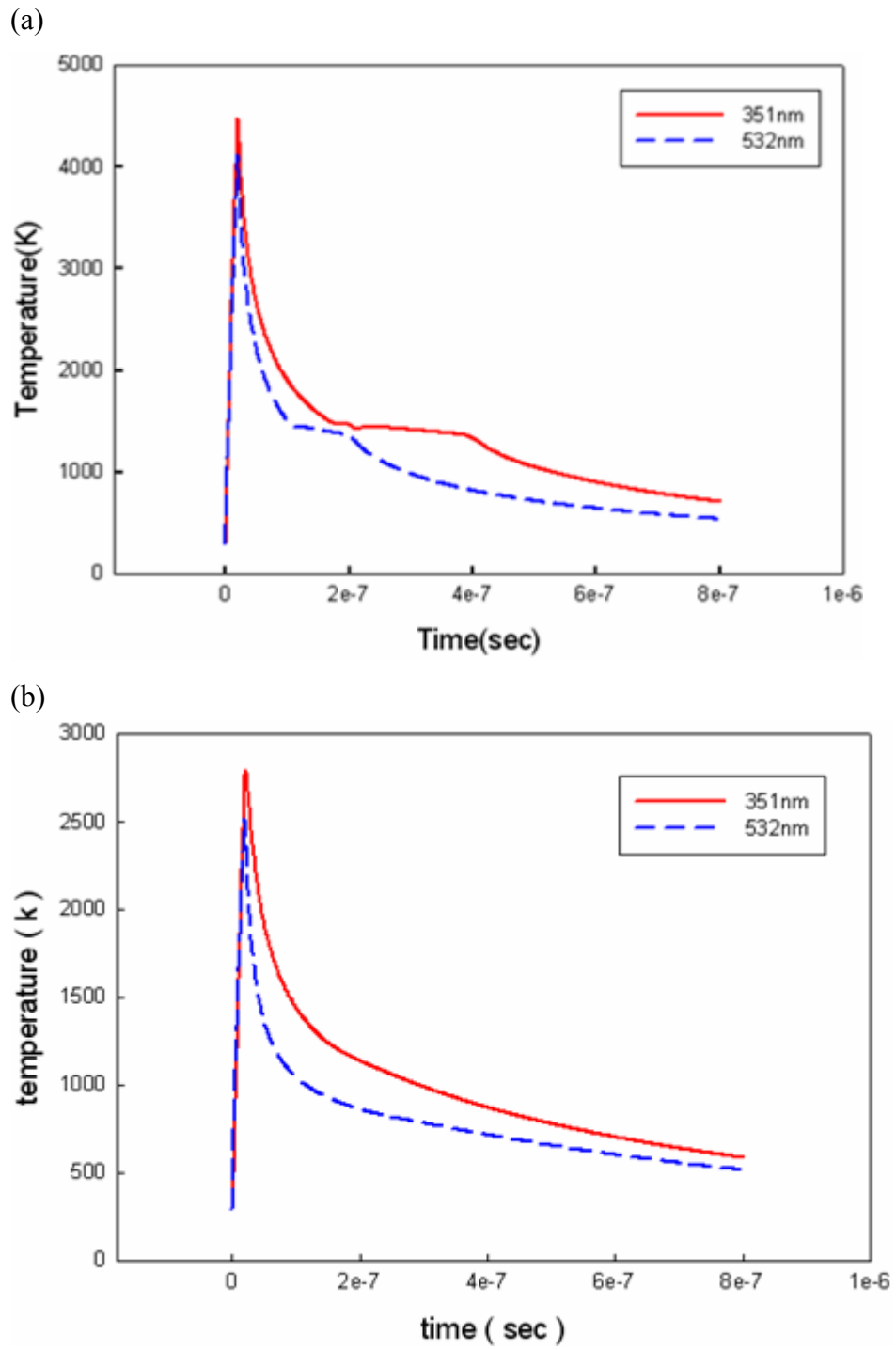Fig.4-1 The absorption coefficient on different material

(a)

(b)

Fig.4-2 The temperature curve versus the time with different laser wavelength on (a) silicon film (b) a-C:H film.